Journal of Alloys and Compounds 1055 (2026) 186509

Contents lists available at ScienceDirect

Journal of Alloys and Compounds

journal homepage: www.elsevier.com/locate/jalcom

Detailed microstructural analysis and hydrogenation performance of ball-milled nanocrystalline MgH_2 powders co-catalyzed by $FeTiH_2$ and GO

Roman Paramonov [a], Gábor Ribárik [a], Viktória Kovács-Kis [b,c], János Kele-Jókuthy [d], Zoltán Novák [d], Zoltán Dankházi [a], Stanislava Todorova [e], Tony Spassov [e,f], Ádám Révész [a,*]

[a] Department of Materials Physics, Institute of Physics, Eötvös University, P.O.B. 32, Budapest H-1518, Hungary
[b] HUN-REN Centre for Energy Research, Konkoly-Thege Miklós u 29-33, Budapest, Hungary
[c] Department of Mineralogy, Eötvös University, Pázmány Péter sétány 1/c, Budapest H-1117, Hungary
[d] MTA-ELTE "Lendület" Catalysis and Organic Synthesis Research Group Institute of Chemistry, Eötvös Loránd University, Hungary
[e] Department of Chemistry, University of Sofia "St.Kl.Ohridski", Sofia 1164, Bulgaria
[f] National Centre of Excellence Mechatronics and Clean Technologies, 8 Kliment Ohridski Blvd., Sofia 1756, Bulgaria

ARTICLE INFO

Keywords:
Hydrogen storage
Magnesium
Severe plastic deformation
Ball-milling
X-ray Line profile analysis

ABSTRACT

High-energy ball-milling technique was employed to synthesize a series of MgH_2 – based composite powders containing 30 wt% Fe – TiH_2 milled solution as a catalyst and graphene oxide as a co-catalyst. Milling durations of 1 h, 3 h and 10 h were investigated. The morphology of the as-milled powders was examined by scanning electron microscopy and transmitting electron microscopy, while their microstructural characteristics were analyzed by X-ray diffraction. Convolutional Multiple Whole Profile fitting algorithm was applied to quantify the microstructural parameters of the powders. Prolonged milling time resulted in a pronounced reduction in powder aggregate size, accompanied by a decrease in the coherently scattering crystallite size to approximately 7 nm. Concurrently, severe plastic deformation induced a very high dislocation density ($\sim 10^{16}$ nm^{-2}). The dehydrogenation behavior of the composites was studied by differential scanning calorimetry, revealing that the addition of graphene oxide significantly lowers the hydrogen desorption temperatures. Hydrogen sorption kinetics measured using a Sieverts-type apparatus demonstrated that the composite milled for 3 h exhibits the most rapid hydrogen absorption and desorption behavior.

1. Introduction

As global energy demand continues to rise, interest in renewable energy sources has increased correspondingly. Nevertheless, the integration of these clean energy sources to the existing energy grid is still hindered due to their strong spatial and temporal condition dependence [1]. In this context hydrogen emerges as a potential candidate with expected usage growth of 50 % by 2030 [2]. Within the conceptual framework of a "hydrogen economy", hydrogen primarily functions as an energy carrier [3], owing to its abundance and exceptional energy storage capacity in its molecular state, which seamlessly integrates with renewable energy sources [4,5]. Despite these advantages, hydrogen storage faces significant challenges that hinder its widespread commercial adoption [6]. Conventional storage techniques, including storage in liquid and gaseous form, give a raise to safety concerns, involve unavoidable energy loss during exploitation among other known issues [7–9]. On the other hand, desired goals of safety, gravimetric and volumetric energy density can be attained through the implementation of solid-stage hydrogen carrier units [10,11]. In the last couple of decades, intensive research efforts have focused on developing efficient solid-state hydrogen storage systems that combine high hydrogen density with practical applicability, addressing both fundamental and applied aspects [12,13].

Among the diverse hydrogen storage systems, metal hydrides gained outstanding potential [14], including a particular interest to magnesium and its hydride due to supreme gravimetric hydrogen capacity and satisfactory cyclic stability [15–17]. Magnesium exhibits the highest theoretical gravimetric hydrogen capacity of all metals (7.6 wt% or 2600 Wh/kg) [18]. In addition, this metal is light, low cost, abundant in the Earth's crust, and non-toxic [12,14–17]. Despite these advantages, the commercial application of magnesium for hydrogen storage is hindered by its sluggish kinetics and high hydrogenation/dehydrogenation

* Corresponding author.
E-mail address: revesz.adam@ttk.elte.hu (Á. Révész).

https://doi.org/10.1016/j.jallcom.2026.186509
Received 8 December 2025; Received in revised form 24 January 2026; Accepted 28 January 2026
Available online 29 January 2026

enthalpy [19]. One effective strategy to overcome these limitations is nanostructuring [20–26], which involves a reduction of the crystallite size down to 100–10 nm by intensive deformation techniques such as ball-milling [31]. Nanostructured Mg exhibits larger specific surface area, distorted atomic bonds in the vicinity of grain boundaries, which can promote hydrogen diffusion into the interior of Mg nanocrystals [27–30].

High energy ball milling (HEBM) is a prevalent technique for producing nanostructured hydrogen storage materials [26]. This approach applies substantial energy to powders via severe plastic deformation (SPD), markedly increasing the grain boundary volume fraction and the density of other lattice defects, including dislocations [31−35]. These defects evidently promote faster hydrogen sorption kinetics due to the enlarged diffusion length of the hydrogen [36–38]. Ab initio molecular dynamics and density functional theory have shown that nanoclusters are thermodynamically less stable than bulk MgH_2 with a reduced formation energy resulting in weakened Mg–H bonds [39].

Furthermore, the absorption kinetics of Mg/MgH_2 and the temperature of hydrogen sorption can be significantly enhanced by alloying Mg with different elements [40–42]. The high Mg–H bonding energy which underlies the thermal stability of MgH_2 can be reduced through the introduction of transition metals (TMs), forming Mg–TM–H bonds [43]. For example, the addition of different TM catalysts, including Ti [44–46], Fe [47,48] and Ni [49–53], or transition metal oxides [54–60], high entropy alloys [61], carbon nanostructures [62] and various synergetic catalyst combinations [54,63–67] has been demonstrated to improve desorption kinetics, cyclic life stability, and activation energy of Mg-based hydrogen storage systems.

FeTi, a widely studied transition metal combination is often applied as a primary hydrogen storage material, either as a solid solution or intermetallic compound [68–73], and as an efficient catalyst for MgH_2 [44,74–77]. Ball-milled MgH_2 – FeTi composites have been shown to exhibit a rapid kinetics at elevated temperatures [74,75,78], while, the strong catalytic effect of FeTi leads to a drastic reduction of the activation energy, enabling appreciable hydrogen uptake even at room temperature [79]. Notably, hydrogen release in this system can be initiated at 180 °C [77]. However, achieving reasonable kinetics and conversion at low temperatures typically requires a relatively high catalyst content of approximately 50 wt% [80]. Additionally, an optimal HEBM time of around 3 h has been identified to maximize the overall hydrogen storage performance of MgH_2–FeTi composites [75]. The primary advantage of FeTi becomes evident for large-scale applications, owing to its excellent price-to-performance ratio compared with TiMn and Nb_2O_5 [73].

In addition to TMs, carbon nanostructures have been extensively investigated as catalysts and co-catalysts for MgH_2 in recent years [62,81–85]. Graphene (Gr) exhibit notable catalytic activity in MgH_2 [86], however, conventional catalysts clearly outperform pure graphene in terms of kinetic enhancement [84]. It has been shown that the most effective use of graphene and other carbon allotropes is as co-catalysts alongside metal-based catalysts. For instance, the incorporation of carbon nanotubes as a co-catalyst improves both the hydrogen sorption kinetics [87] and the cyclic stability of the composite [77]. A similar effect is observed when graphene is introduced as a co-catalyst, as exemplified by the MgH_2–Ti–Ni–Fe@Gr composite, which exhibits a substantial reduction in desorption onset temperature and enhanced cyclic stability compared to the Gr-free MgH_2–Ti–Ni–Fe alloy [44]. The pronounced improvement in cyclic stability is attributed to anchoring of the catalyst particles on the Gr surface, which prevents aggregation of both MgH_2 and transition metal particles [83].

Graphene oxide (GO), which is often used as a precursor for a specific form of graphene (rGO) [82,83,88] has been less commonly reported as a co-catalyst for MgH_2. Nevertheless, its synergistic interaction with metal oxides, such as SnO_2 can significantly reduce the hydrogenation onset temperature. For example, ball-milled GO supported MgH_2–SnO_2 composite exhibit an onset temperature of 274 °C, compared to 290 °C for the GO-free counterpart [89], highlighting the potential of GO as an effective co-catalyst.

In the current research nanocrystalline MgH_2 powders have been co-catalyzed with FeTiH and GO by HEBM for varying durations. The catalyst content was set as high as 30 wt%, since high FeTi may drastically improve high temperature kinetics. GO was selected as a co-catalyst because, while it possesses a morphology similar to graphene in the form of 2D sheets or flakes, it exhibits distinct chemical properties and represents a more cost-effective alternative. The study focuses on the microstructural, morphological and thermal evolution of the powders during milling and set up correlation between their structural parameters and hydrogen storage performance.

2. Materials and methods

2.1. Sample preparation

As a first step of powder processing, FeTiH catalyst was synthesized via ball-milling of pure Fe and TiH_2 powders (purity 99.9 %) at a 1:1 wt ratio. The HEBM process has been carried out in SPEX 8000 M Mixer Mill (SPEX, Metuchen, NJ, USA) using a stainless-steel vial (volume: 65 ml) containing 10 stainless steel balls (1/4 in) with 10:1 ball-to-powder ratio at an operational frequency of 1425 RPM. The milling time was set as 10 h in order to achieve a complete homogenization of the catalysts, in accordance with our previous studies [75,90].

In the subsequent step, the mixture of as-milled FeTiH powder (97 wt %) and GO (3 wt%) (4–10 % edge-oxidized, 15–20 layers; Sigma-Aldrich, St. Louis, MO, USA) diluted with dimethyl-formamide (DMF) solution was subjected to ultrasonication in a water bath using a Bransonic MH5800H-E Heated Ultrasonic Cleaning Bath (Branson Ultrasonic, Danbury, USA) for 5 h in order to ensure proper distribution of the components and cohesion between FeTiH and GO particles.

In the final step, the obtained FeTiH/GO co-catalyst (30 wt%) was further co-milled with MgH_2 powder (90 % MgH_2, remainder Mg; Sigma-Aldrich, St. Louis, MO, USA; CAS-number: 7693–23–8) for 1, 3 and 10 h with 10:1 ball-to-powder ratio. Hereafter, these composite blends will be denoted as MgH_2 + FeTiH/GO (1 h), MgH_2 + FeTiH/GO (3 h), MgH_2 + FeTiH/GO (10 h). For comparison, a reference MgH_2 powder was also synthesized in the ball mill, hereafter it is denoted as MgH_2 (3 h). All powder processing has been carried out under protective Ar atmosphere in a glove box. To prevent powder sticking to the vial walls, the milling process was interrupted after one hour, and the vial was rotated by 90 ° along its symmetrical axis.

2.2. Microstructural characterization

2.2.1. Scanning electron microscopy

Detailed morphological studies on the MgH_2 (3 h) and MgH_2 + FeTiH/GO powders were carried out in a FEI QUANTA 3D dual beam scanning electron microscope (SEM) via back-scattered electron (BSE) and secondary electrons (SE) regimes. The chemical composition was evaluated by energy-disperse X-ray spectroscopy (EDS) with 1 % relative accuracy. Quantitative analysis of the powder agglomerates was carried out by ImageJ software by obtaining the individual length of each particle through their geometrical center in the same direction.

2.2.2. Transmitting electron microscopy

For transmission electron microscopy experiments, the HEBM powders of the as-milled FeTiH/GO catalyst and MgH_2 + FeTiH/GO (3 h) composite were dispersed dry on a lacey carbon coated Cu TEM grid (Ted Pella). TEM analysis was carried out using an FEI Themis G2 Cs corrected microscope (FEI, Thermo Fischer, Schottky FEG electron source, 200 keV acceleration voltage, 0.08 nm resolution in high resolution (HRTEM) mode and 1.6 nm resolution in scanning (STEM) mode). TEM images were recorded with Velox software (Thermo Fischer). High-angle annular dark-field (HAADF) technique was applied to explore the atomic number (Z) contrast of the powders on nanoscale. Elemental

maps are plotted using the net count after removing the background. For background calculation, the Brown-Powell ionization cross section model implemented in the 3.8.1 offline version of the Velox software was used. To improve visualization, 5px Gaussian blur was applied post filtering.

2.2.3. X-ray diffraction

Phase analysis and the microstructure of the MgH_2 + FeTiH/GO composites and MgH_2 (3 h) reference powder was investigated by X-ray powder diffraction (XRD). All measurements were carried out on a Rigaku SmartLab diffractometer in a Bragg–Brentano geometry using Cu-Kα radiation. The data were collected in the range $2\theta = 20°–90°$ with a step size of $\Delta(2\theta) = 0.01°$. For detailed microstructural analysis, the recorded XRD patterns were evaluated by the Convolutional Multiple Whole Profile (CMWP) fitting analysis, see Supplementary material.

2.3. Thermal characterization

Linear-heating scans were performed on a power-compensated Perkin Elmer Differential scanning Calorimeter (DSC) to explore the thermal stability and hydrogen release of the powder composites at heating rates 10 K/min, 20 K/min, 40 K/min and 80 K/min. All measurements were carried out in a Pt sample holder under constant high-purity Ar flux. Temperature and enthalpy were calibrated by the melting of pure In and Al. The activation energy (E_a) of the dehydrogenation processes has been determined by the Kissinger analysis [91]:

$$\frac{\beta}{T_i^2} = \frac{Z_i R}{E_{a,i}} \exp\left(\frac{-E_{a,i}}{RT_i}\right) \quad (1)$$

where T_i denotes the individual transformation peak temperatures, Z and *R* are the frequency factor and the gas constant, respectively. Plotting $\ln(\beta/T_i^2)$ vs. T_i^{-1} enables the determination of E_a for each transformation from the slope of the fitted straight line.

2.4. Hydrogen storage experiments

The hydrogen-storage performance of all powder composites were carried in a home-made Sieverts'-type apparatus. Isothermal hydrogenation and dehydrogenation measurements were performed at 573 K, with an initial hydrogen pressure of 1 MPa for absorption and 1 kPa for desorption. Linear heating up to the sorption temperature was done in vacuum, followed by the introduction of hydrogen into the sample chamber (the pre-set hydrogen pressure was reached in a few seconds). For each experiment, approximately 100 mg of powder was used.

3. Results

The TEM analysis presented in Figs. 1 and 2 summarizes the characteristic sub-micrometer-scale features of the as-milled FeTiH/GO catalyst. As shown in Fig. 1a, catalyst nanoparticles mostly form aggregates with sizes reaching several hundred nanometers. These aggregates are completely wrapped by GO additive, which is attached to the particle surfaces and interconnects individual catalyst aggregates into larger units (Fig. 1a). Individual packets of GO sheets with thickness of 3–10 nm are clearly observed on the HRTEM images in edge view (denoted by white arrows in Fig. 1b) together with packets of sheets in plane view. These observations indicate that GO is randomly oriented and, on average, form isotropic 3D clusters on the mesoscale, as also supported by the corresponding Fourier transform shown in the inset of Fig. 1a. In certain regions, individual FeTi nanoparticles overlaying GO aggregate can also be identified (Fig. 1c). The presence of few nm thick GO packet surrounding the nanoparticle (white arrow in Fig. 1c) indicates a close and stable nanoscale connection between the two components. According to EDS elemental maps, the catalyst nanoparticles consist of a homogeneous mixture of Fe and Ti (Fig. 1d-e).

Fig. 2 shows some individual catalyst nanoparticles attached to the surface of a large and thick GO aggregate. This image was acquired in STEM–HAADF mode, in which the contrast is directly proportional to the average atomic number of the material, in case of uniform thickness. Owing to the large Z difference between GO and the FeTiH catalyst nanoparticles, the latter can be clearly distinguished despite the presence of the underlying thick carbonaceous substrate. The marked region in Fig. 2a shows contrast variation within the GO substrate (see inset), which can be attributed to positional thickness variation. At the same time, individual catalyst nanoparticles with sizes of approximately 10–20 nm (bright spots in the inset) are still recognizable. This region has been subjected to EDS mapping (Fig. 2b-d). As revealed by the EDS analysis, some nanoparticles contain only Fe, while others consist of a mixture of Fe and Ti. This finding indicates that the elemental distribution of Fe and Ti within the individual nanoparticles is inhomogeneous on the nanometer scale (Figs. 2c and 2d). This observation implies

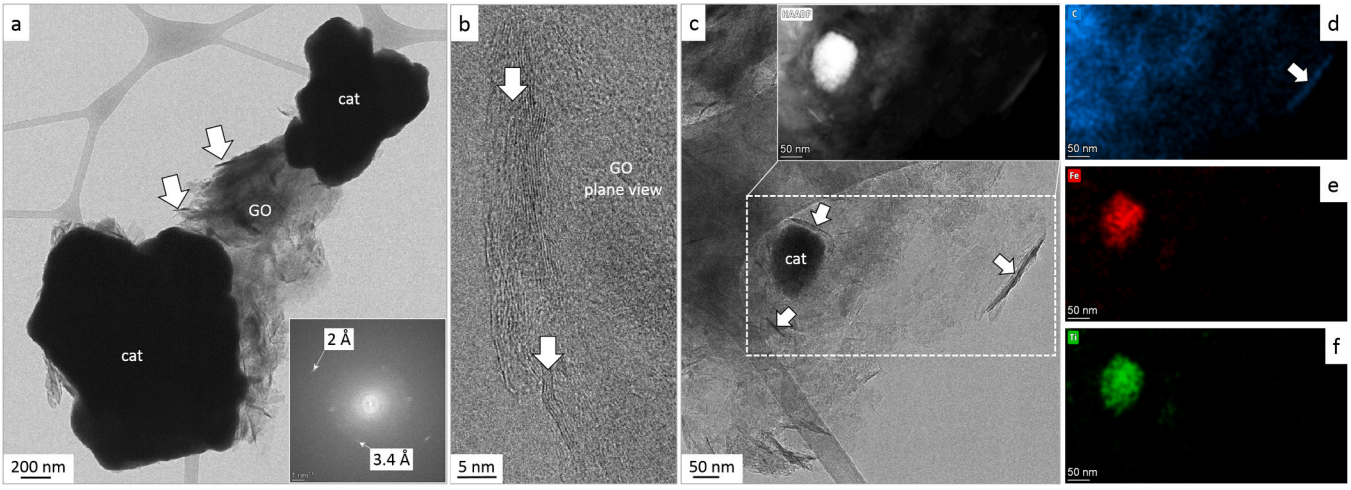

Fig. 1. (a) Bright field (BF) TEM image of aggregates of FeTiH catalyst nanoparticles (cat) surrounded and connected by GO. The inset shows the Fast Fourier Transform (FFT) of a GO aggregate. The presence of reflections from both in plane periodicity (2 Å) and from the distance between layers (3.4 Å) indicates that the GO aggregate is randomly oriented. White arrows indicate GO sheets viewed from the edge. (b) HRTEM image of a GO aggregate showing edge view (arrow) and plane view GO sheets in close vicinity. (c) BF image of a single catalyst nanoparticle overlaying on a GO aggregate. In the inset a HAADF image of the marked area is shown. White arrows show GO sheets in edge view. EDS elemental maps showing the spatial distribution of (d) C, (e) Fe and (f) Ti, respectively, of the area indicated on (c).

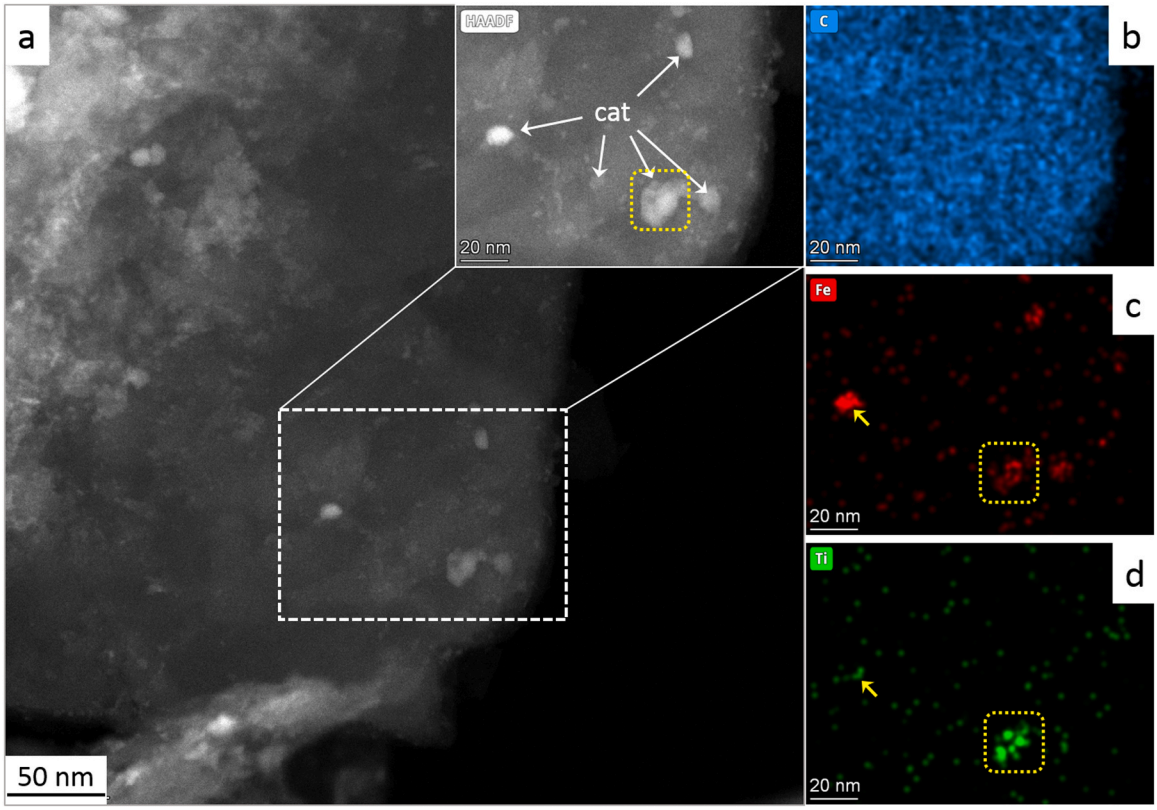

Fig. 2. (a) HAADF image of a GO aggregate with catalyst nanoparticles (cat) attached to its surface. EDS elemental maps showing the spatial distribution of (b) C, (c) Fe and (d) Ti, respectively, of the area indicated on (a). Inhomogeneous distribution of Fe and Ti inside catalyst nanoparticles is highlighted with yellow arrows and boxes.

that larger catalyst nanoparticles (~50 nm) that appear compositionally homogeneous (e.g. the one marked in Fig. 2c) are in fact, composite particles built up from Fe-rich and Ti-rich rich units with characteristic sizes of ~10 nm or smaller. At the same time, the observed common aggregation of catalyst nanoparticles results in an overall homogeneous composition on the mesoscale.

SEM-BSE images of the MgH_2 + FeTiH/GO powder composites are presented in Fig. 3. Powder- to-ball and powder-to-vial interactions evidently lead to the formation of flat-surfaced particles, which can be attributed to the relative softness of MgH_2 compared to the stainless-steel milling environment. The BSE imaging mode provides atomic number contrast, from which it can be inferred that the catalyst is evenly distributed throughout the composite even after 1 h of HEBM. As observed in the images, FeTiH particles are notably smaller than the MgH_2 aggregates and show a pronounced tendency to become embedded in softer MgH_2 clusters. Consequently, the structure of the catalyzed material can be described as FeTiH particles reinforcing MgH_2 aggregate matrix. The SEM–BSE images were further employed for quantitative analysis of the MgH_2 aggregate size distribution. Particle sizes were determined by measuring the horizontal and vertical dimensions through the geometric center of each aggregate. In agreement with recent studies [92], the collected data can be satisfactorily fitted by a lognormal function, with the maximum located at approximately 2 μm.

According to the fitted distributions, the median (m_{SEM}), variance (σ_{SEM}) and area-weighted mean agglomerate size ($\langle d \rangle_{SEM,area}$) decrease with increasing milling time. The pronounced reduction of these parameters indicates that longer milling durations promote more effective structural refinement within a reasonable processing time frame. A notable discrepancy is observed between the reference MgH_2 (3 h) sample and MgH_2 + FeTiH/GO (3 h). Although the median for the reference sample is comparatively larger, the presence of the catalyst promotes to the formation of larger aggregates, thereby resulting in broader variance. Similar phenomena was also observed in a previous study [69]. Evidently, increasing catalyst content leads to larger variance and area weighted average particle size. The FeTiH particles presumably act as nucleation sites for aggregate formation. The relatively soft MgH_2 phase tends to accumulate around the structurally stable catalyst particles, which ultimately results in substantial size inhomogeneity within the composite.

The EDS spectra illustrated in Fig. 3 provide quantitative information on the chemical composition of the MgH_2 + FeTiH/GO composites. While Fe:Ti ratio remains close to initial Fe and TiH mixture composition (see Table 1), the Mg:FeTi ratio increases continuously with milling time (20 wt% for MgH_2 + FeTiH/GO (1 h), 24 wt% for MgH_2 + FeTiH/GO (3 h) and 27 wt% for MgH_2 + FeTiH/GO (10 h)). Accordingly, the nominal FeTi content (28.65 wt%) is achieved only after prolonged milling. These observations are consistent with previous studies [74,75].

Fig. 4 summarizes the TEM analysis of the MgH_2 + FeTiH/GO (3 h) composite. As shown in Fig. 4a, the FeTiH catalyst mostly consists of rough-edged aggregates of several hundred nanometers. Notably, no underlying GO substrate is observed in these regions. The HAADF image (inset of Fig. 4a) reveals that the catalyst aggregates are either attached to or embedded within thick MgH_2 crystals. The elemental maps presented in Fig. 4b-d confirm that the surface of the soft MgH_2 crystal is not completely depleted in Mg, indicating that a fraction of the harder FeTi catalyst particles can be embedded within hydride aggregates. In addition to the large FeTi particles, individual nanometer-sized catalyst can also be identified. According to the elemental maps, the distribution of Fe and Ti is uniform both within the large aggregates and in the individual particles (Fig. 4b-d).

Fig. 5a presents the XRD pattern of the FeTiH catalysts HEBMed for 10 h. It is seen that the pattern is dominated by broad and diffuse halos which indicate the formation of amorphous and nanocrystalline

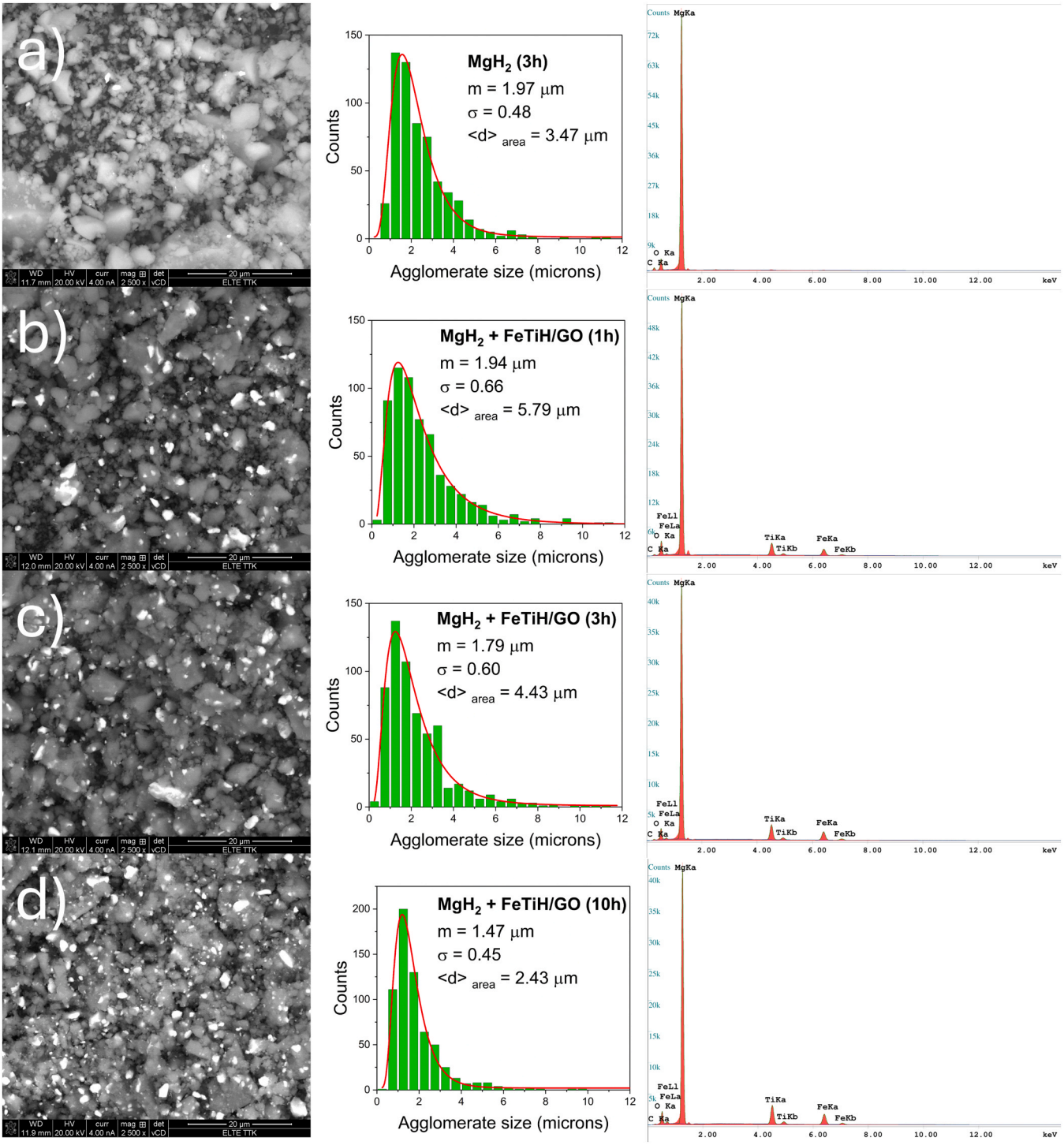

Fig. 3. Low magnification BSE-SEM images of ball-milled a) MgH_2 (3 h), (b) MgH_2 + FeTiH/GO (1 h), (c) MgH_2 + FeTiH/GO (3 h) and (d) MgH_2 + FeTiH/GO (10 h) samples with corresponding particle size distribution histograms fitted by lognormal function and the respective EDS spectra.

intermetallic FeTi. Notably, the characteristic Bragg-reflections of bcc-Fe and cubic TiH_2 are absent, in agreement with the Fe-Ti particles observed in the HRTEM images, see Figs. 1 and 2. It is noted that the size of the coherently scattering nanocrystalline domains of the Fe-rich aggregates presented in Fig. 2 is below the detection limit of conventional X-ray powder diffractometry.

The 1:1 Fe:TiH_2 weight ratio employed in this study offers several advantages. First, the observed large FeTi amorphous fraction can provide multiple pathways for hydrogen diffusion [93]. Second, the nominal Fe:Ti ratio is close to that of the intermetallic compound, as confirmed by its 2Θ position in the XRD pattern (Fig. 5a). This compound not only can store hydrogen, but can also facilitate the "hydrogen pump" effect, thereby accelerating hydrogen distribution within the composite [76]. Furthermore, the small amount of unreacted TiH_2 may contribute to a reduction in the activation energy for hydrogenation and dehydrogenation reactions [94].

The X-ray diffractograms of the as-milled reference MgH_2 powder and the MgH_2 + FeTiH/GO composites are depicted in Fig. 5b. All patterns are dominated by the Bragg-peaks of tetragonal α-MgH_2, however, a metastable γ-MgH_2 phase, which forms under high pressure,

Table 1
Elemental composition of MgH_2 + FeTiH/GO composites obtained from the EDS analysis.

	MgH_2 + FeTiH/GO (1 h)	MgH_2 + FeTiH/GO (3 h)	MgH_2 + FeTiH/GO (10 h)
Mg (wt %)	80.1	76.4	73.1
Fe (wt %)	10.2	12.4	14.1
Ti (wt %)	9.7	11.2	12.8

is also present in small amount in each powder. As a consequence of SPD during HEBM, all reflections exhibit pronounced broadening, corresponding to intensive crystallite size refinement [29,36,95]. Notably, the intensity ratio between the strongest γ-MgH_2 and α-MgH_2 reflections is the highest for the pure MgH_2 powder, indicating that the collisions between the hardened stainless-steel balls and the MgH_2 powder particles induce the most intensive plastic deformation among all powders. In contrast, this ratio is reduced for the co-catalyst containing composites, suggesting that the presence of FeTiH/GO mitigates the impact intensity between the hydride particles and the milling balls. As seen, a reflection centered at $2\theta = 43$ deg is observed in all patterns and can be attributed to the formation of some MgO. It is also evident from the patterns that no reflections of any Fe-Ti-H phase are detected, which is consistent with the amorphization of this catalyst in the solid state, approved by the overlapping broad halo developed at around $2\theta = 44$ deg. Similar phenomenon has been reported for HEBM MgH_2 catalyzed by increased amount of activated FeTi [74].

Fig. 6 summarizes the application of the CMWP algorithm to the measured XRD profiles of the nanocrystalline MgH_2 powder and all three MgH_2 + FeTiH/GO composites. Each graph presents the fitted diffraction profile together with the difference between the measured data and the corresponding fit. It is undoubted from the plots that the convolutional numerical algorithm has perfectly converged after approximately 100 iteration steps, yielding excellent fit for all powders. The microstructural parameters obtained from the CMWP analysis, such as the median (m) and variance (σ) of the main coherently scattering α-MgH_2 crystallites are also depicted in each graph. For the reference MgH_2 powder, the m value is the largest, corresponding to larger nanocrystals. Upon milling the co-catalyst to MgH_2 for 1 h, the σ value shows a slight increase. Subsequent HEBM time results in a gradual decrease of the variance, the smaller σ refers to a more homogeneous nanostructure. The corresponding G(x) lognormal size-distribution functions for the tetragonal α-MgH_2 phase obtained from Eq. S4 are plotted for all composites in Fig. 7. It is evident that all powders are characterized by fine nanometric crystalline domains that formed by SPD during the milling process. The pure MgH_2 exhibits a slightly broader and more inhomogeneous size distribution, whereas the addition of the FeTiH/GO co-catalyst to MgH_2 shifts of the distribution towards smaller values, indicative of a more homogeneous nanostructure.

Based on Eq. S5, the $\langle D \rangle_{area}$ area averaged crystallite sizes were also determined. These values are plotted in Fig. 8a and are indicated by triangular symbols on the histograms in Fig. 7. As shown, all MgH_2 coherently scattering domain sizes are in the nanometric regime, reflecting extensive nanocrystallization during ball milling, in agreement with previous reports on other Mg-based nanopowders processed by HEBM [36,75,95]. The pure MgH_2 nanopowder exhibits an average value of $\langle D \rangle_{area} = 7$ nm, which is practically the same for the MgH_2 + FeTiH/GO (1 h) composite. Prolonged milling leads only a marginal further reduction to approximately 6 nm. Such nanocrystalline powders are abundant in high angle grain boundaries characterized by distorted atomic bonds and reduced atomic density [32]. The volume fraction of these two-dimensional lattice defects can reach as high as 20–30 % and

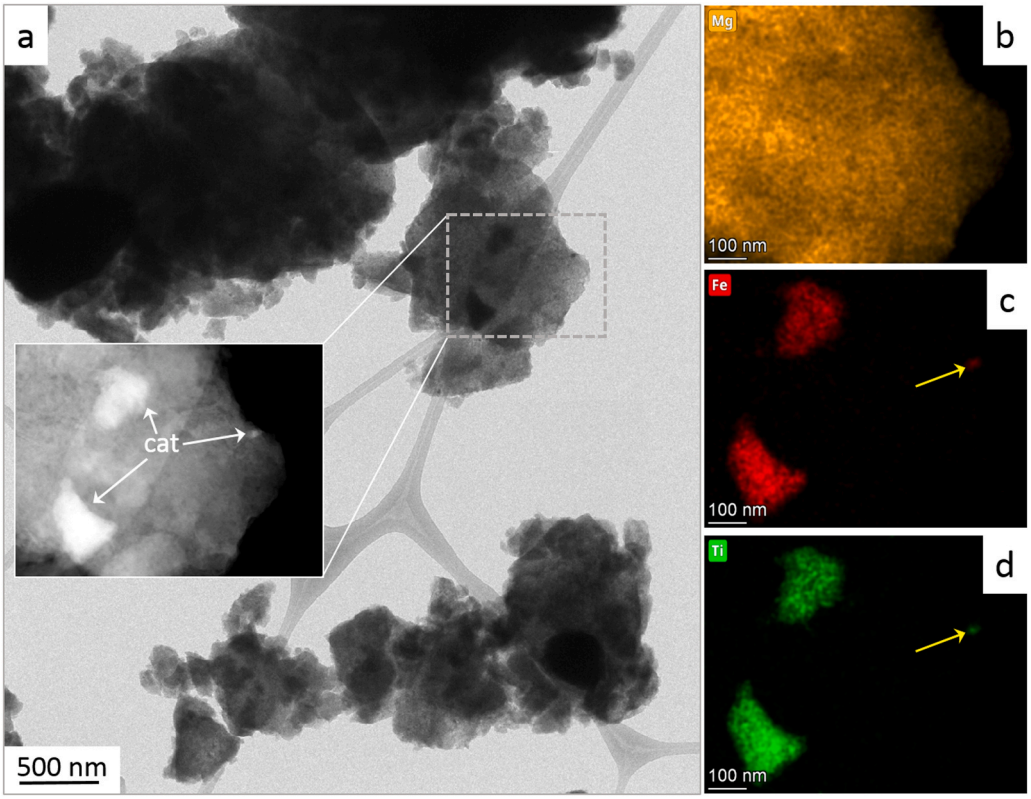

Fig. 4. (a) Typical BF image of sample MgH_2 + FeTiH/GO (3 h). In the insert the HAADF image of the marked area is shown. Catalyst nanoparticles and their aggregates (cat) are recognizable due to their higher brightness. EDS elemental maps showing the spatial distribution of (b) Mg, (c) Fe and (d) Ti, respectively, of the area indicated in (a). Yellow arrows point to an individual catalyst nanoparticle.

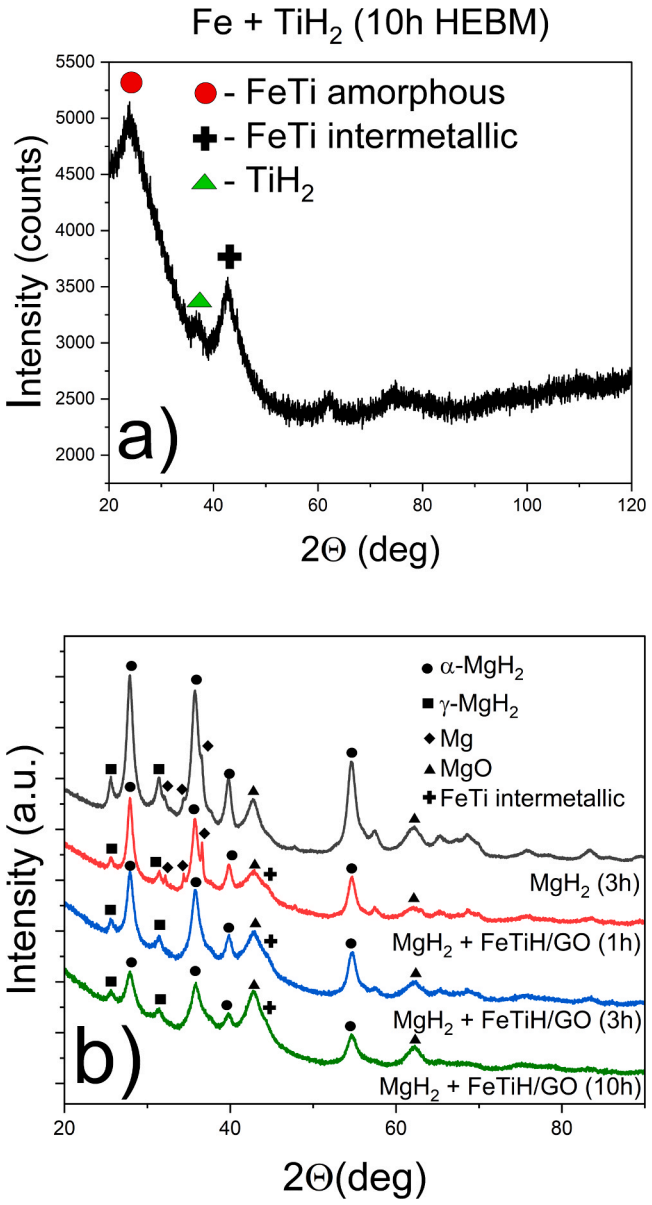

Fig. 5. XRD patterns of the (a) as-milled FeTiH catalyst and (b) the HEBM MgH_2 and MgH_2 + FeTiH/GO composites.

can act as fast penetration channels for hydrogen. It should be noted that the crystallite size obtained from CMWP X-ray line profile analysis cannot be directly compared with the crystallite size estimated from HRTEM images, as the former is typically smaller, particularly in materials processed by SPD. This discrepancy arises because the coherently scattering domains are bounded by grain boundaries rich in dislocations or dipolar walls [96].

It is noted that a clear correlation is observed between the powder particle size obtained from the SEM images (Fig. 3) and the coherently scattering crystallite size obtained from the CMWP analysis (Fig. 8a); specifically, longer SPD duration leads to simultaneous structural refinement on both the micron and nanoscale. Based on the data presented in Figs. 3 and 8a. it can be estimated that a single powder aggregate contains, on average, on the order of 10^7 coherently scattering nanocrystalline domains.

In addition to nanostructural refinement, one-dimensional lattice defect such as dislocations can also form during SPD within Mg-based powder particles [29,36,75]. Fig. 8b presents the average dislocation density (ρ) values for the main α-MgH_2 phase obtained from the CMWP analysis for all processed powders. As one can notice, HEBM results in a very high value ($\rho \sim 5 \cdot 10^{15}$ m^{-2}) for the as-milled MgH_2 nanopowder. The addition of the FeTiH/GO co-catalyst leads to a further increase in the dislocation density, exceeding $\rho \sim 10^{16}$ m^{-2} (which is close to the theoretical limit) and may promote hydrogen kinetic enhancement of MgH_2. Based on the obtained ρ values, the average dislocation distance (L_C) can also be calculated using Eq. S6, and is shown in Fig. 8a. As a consequence of the abundant dislocations, the L_C values exhibit nanometric dimensions, however, they are slightly larger than $\langle D \rangle_{area}$ for each composite. This indicates that, on average, fewer than one dislocation is present within an individual nanocrystal, despite the overall extremely high dislocation density.

Fig. 9 presents the continuous heating DSC curves recorded at heating rate of 40 K/min for the MgH_2 + FeTiH/GO composites and the reference sample MgH_2 powder. Each thermogram exhibits two overlapping endothermic peaks (T_1 and T_2), which correspond to the dehydrogenation of the metastable high-pressure γ-MgH_2 and the stable α-MgH_2 phases, in agreement with previous studies [75]. The markedly lower dehydrogenation temperature associated with the γ-MgH_2 → Mg + H_2 reaction in the composite powders is attributed to the weaker Mg-H bond of this hydride phase [75]. The inset of Fig. 9 presents the evolution of the temperature of reaction onset (T_{onset}) as well as T_1 and T_2 as a function of milling time. It is evident from the plot that all characteristic temperatures are significantly reduced in the presence of the FeTiH/GO co-catalyst compared with the as-milled MgH_2 powder. For example, the T_{onset} value for the MgH_2 + FeTiH/GO (1 h) composite decreases by more than 100 °C, while the reduction of the dehydrogenation peak temperatures also exceeds 50 °C. These results clearly demonstrate a synergetic effect between nanocrystalline MgH_2 and the FeTiH/GO co-catalyst. As one can also notice, there exists an increase in the dehydrogenation temperatures with increasing milling time. The lowest T_1 dehydrogenation temperatures of the HEBMed MgH_2 + FeTiH/GO (1 h) powder might relate to the presence of Mg crystallites in the as-received commercial powder (see the XRD pattern in Fig. 6) that can promote the growth of hexagonal Mg during the desorption process without the need for additional nucleation. More extensive attrition and nanocrystallization induced by prolonged millings might reduce this effect, leading to the observed gradual increase of the characteristic temperatures. It is worth noting that the incorporation of FeTiH/GO co-catalyst to MgH_2 results in a substantial reduction of T_2 dehydrogenation temperature compared to GO-free MgH_2 + FeTiH composites [74,75].

The activation energy associated with the T_1 desorption temperature was obtained from the Kissinger-analysis for all powders. As an example, Fig. 10 shows the calorimetric thermograms of the MgH_2 + FeTiH/GO (3 h) composite recorded at heating rates of 10 K/min, 20 K/min, 40 K/min and 80 K/min. The corresponding Kissinger plot shown in the inset exhibits a clear linear relationship. The obtained E_a values for the nanocrystalline MgH_2 powder and the MgH_2 + FeTiH/GO composites are summarized in Fig. 11. The reference MgH_2 powder exhibits a high activation energy (141 kJ/mol), in good agreement with literature value [97,98]. In contrast, a pronounced reduction in E_a is observed for all co-catalyzed powders, with values falling in the range of ~40–100 kJ/mol, rendering them more suitable for practical applications. Among the composites, the MgH_2 + FeTiH/GO (3 h) sample exhibits the lowest value (E_a = 52 kJ/mol), which is almost two times smaller than for MgH_2 + FeTiH/GO (1 h) powder (E_a = 96 kJ/mol). Further extension of the HEBM times leads to an increase in the activation energy, accordingly, the MgH_2 + FeTiH/GO (10 h) composite exhibits a higher value (E_a = 106 kJ/mol). These results indicate that the optimal milling time of approximately 3 h minimizes the dehydrogenation activation energy of MgH_2 + FeTiH/GO powders.

Fig. 12 summarizes the hydrogen sorption performance of the MgH_2 + FeTiH/GO powders. In general, all composites can be hydrogenated and dehydrogenated in a reasonably short time, indicating good kinetics performance. Specifically, the MgH_2 + FeTiH/GO (1 h) powder presents

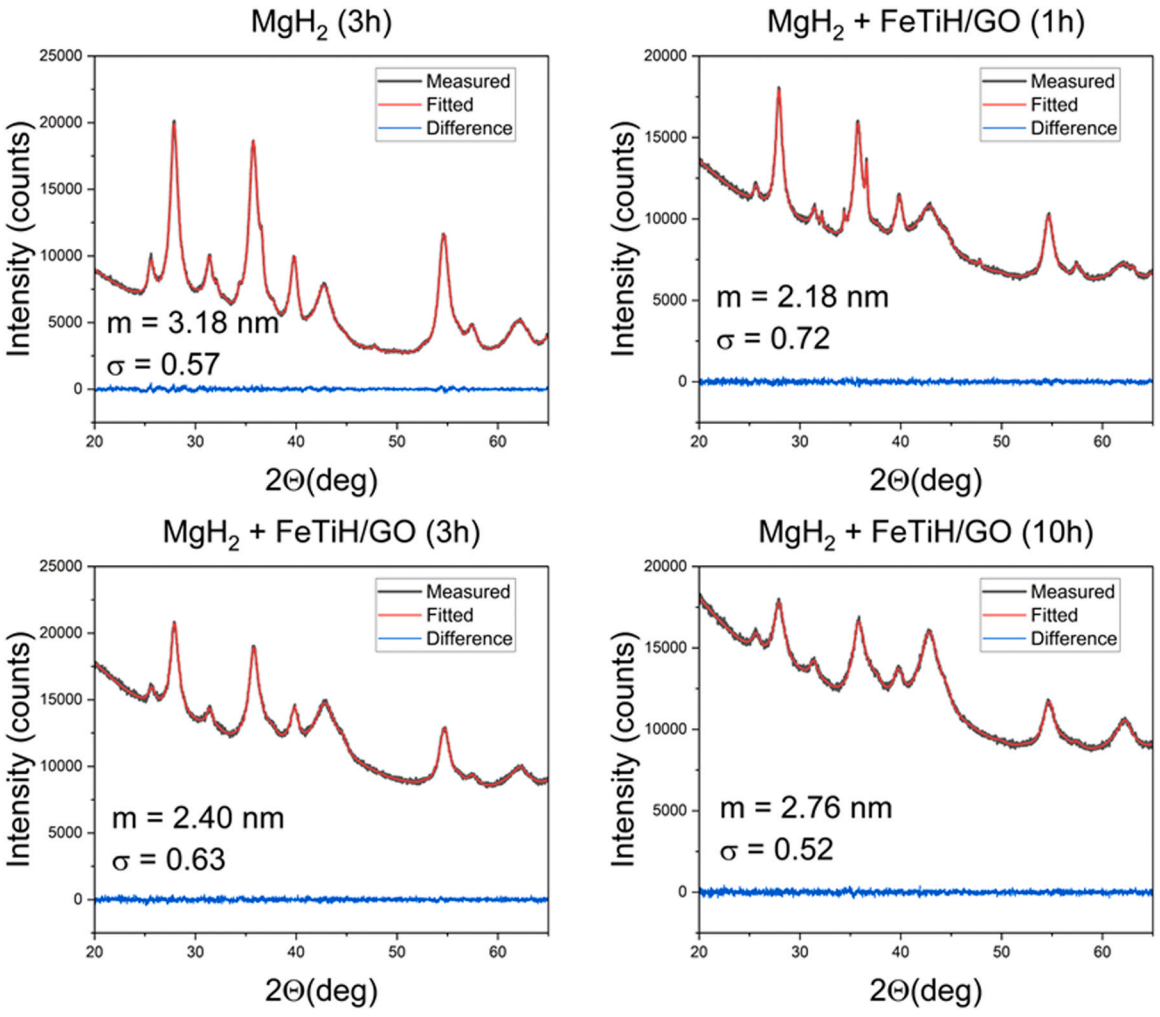

Fig. 6. CMWP fits of the reference MgH_2 and MgH_2 + FeTiH/GO composites. The obtained median (m) and variance (σ) values of the crystallite size distribution functions are also depicted in the respective graphs.

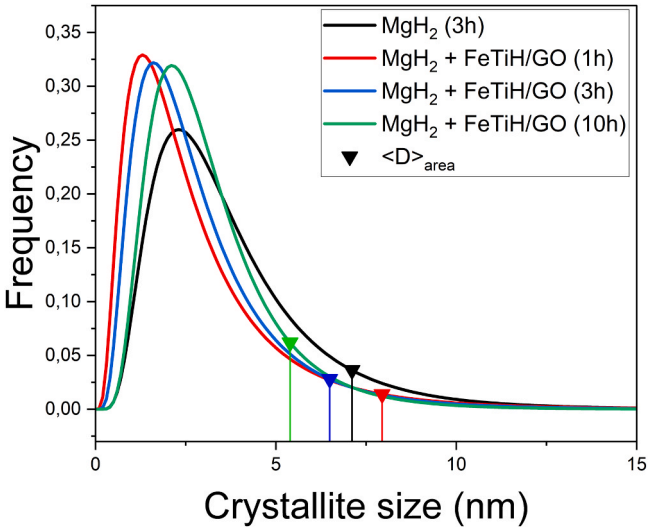

Fig. 7. Lognormal crystallite size histograms for the nanocrystalline MgH_2 and MgH_2 + FeTiH/GO composites. Triangles denote the $\langle D \rangle_{area}$ area averaged crystallite sizes.

a remarkable hydrogen uptake during the 1st (activation) cycle, achieving 50 % of the absorbed hydrogen within 100 s and similar behavior was observed during subsequent runs (see Fig. 12a). As shown in Fig. 12a, longer milling times lead to a deviation between the 1st and 2nd hydrogenation curves, likely due to the gradual formation of a thin oxide layer around the MgH_2 nanocrystals, see also Fig. 6. For instance, the MgH_2 + FeTiH/GO (10 h) sample absorbs more than twice the amount of hydrogen during the second hydrogen uptake. In contrast, the dehydrogenation performance of all powder composites are identical, exhibiting only minor differences between the first and second desorption, see Fig. 12b. Overall, the fastest absorption and desorption are observed for the MgH_2 + FeTiH/GO (3 h) powder, which absorbs 2.3 wt % of hydrogen in 180 s and desorbs 1.3 wt% of hydrogen over the same time interval (see Figs. 12a and 12b). The obtained capacity values for this composite are 3 wt% during absorption and 2.9 wt% during desorption.

The Johnson-Mehl-Avrami model with Kolmogorov extension (JMAK) was employed to gain a deeper understanding of kinetics of the 2nd hydrogenation and dehydrogenation. In brief, this model assumes that the nucleation is a random process, nuclei can emerge on the surface as well as in the bulk [99]. For quantitative analysis, the sorption curves were normalized to their respective maximum capacities. Thereafter, these normalized curves were fitted using the JMAK model function:

$$\alpha(t) = 1 - e^{-kt^n} \quad (2)$$

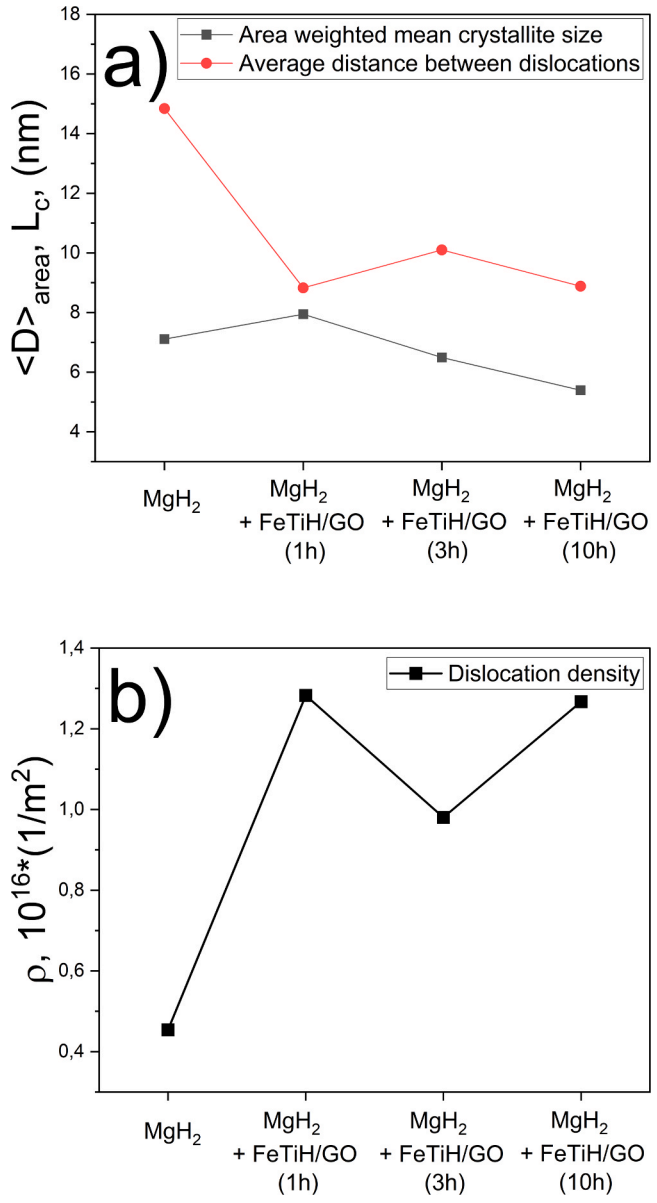

Fig. 8. Structural parameters obtained from the CMPW analysis for nanocrystalline MgH_2 and MgH_2 + FeTiH/GO composites. (a) average crystallite size, average dislocation distance and (b) average dislocation density.

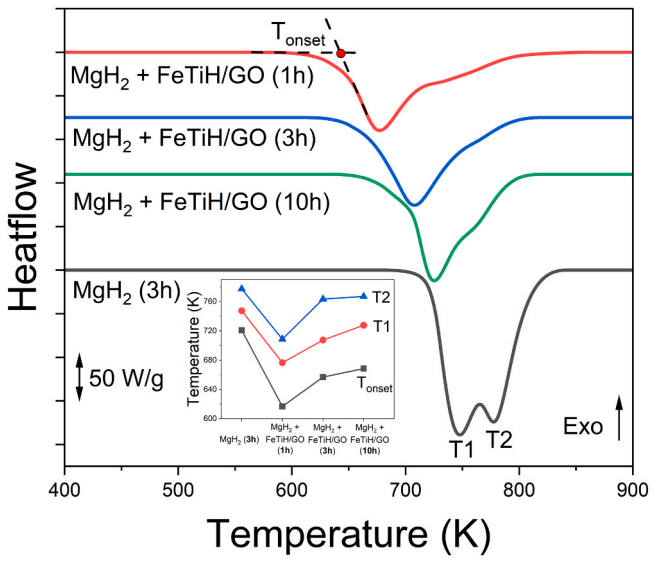

Fig. 9. Linear-heating DSC thermograms of the MgH_2 and MgH_2 + FeTiH/GO powders obtained at heating rate of 40 K/min. The inset shows the variation of the T_1, T_2 and T_{onset} characteristic temperatures as a function of milling time.

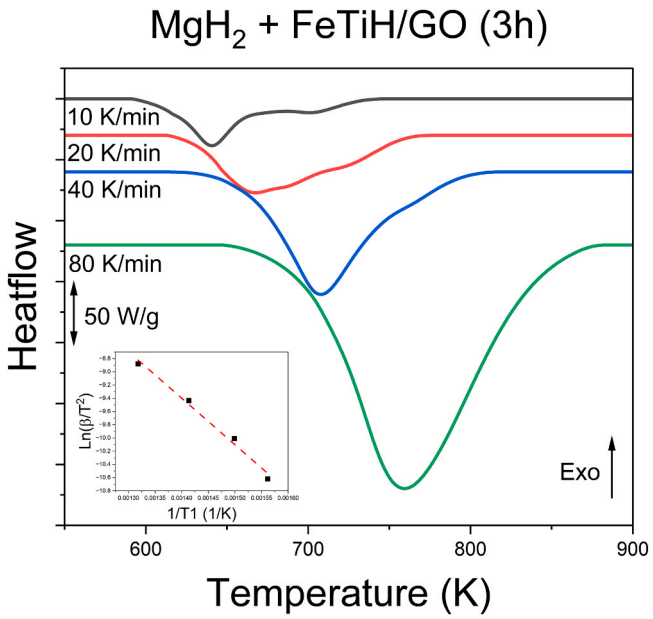

Fig. 10. Dehydrogenation thermograms of the MgH_2 + FeTiH/GO (3 h) powder obtained at different heating rates. The inset shows the Kissinger plot corresponding to the T_1 reaction.

where k is a temperature dependent reaction constant, n is the Avrami exponent that relates to the nucleation and growth mechanism of the new phase [99]. Eq. 2 can be linearized as:

$$\ln(-\ln(1-\alpha)) = n \bullet \ln(t) + \ln(k) \quad (3)$$

By fitting the $\ln(-\ln(1-\alpha))$ term as a function of $\ln(t)$ with a straight line, the slope will provide the n exponent while the intercept with the ordinate gives the k value. As illustrated in the double logarithmic plots in Figs. 13a and 13b, most absorption and desorption curves deviate from a single linear trend predicted by Eq. 3. Nevertheless, each curve can be subdivided into two linear segments, corresponding to a distinct kinetic regimes according to the JMAK fits. As summarized in Table 2, the first absorption stage of MgH_2 + FeTiH/GO (1 h) and MgH_2 + FeTiH/GO (3 h) samples as well as the overall reaction of the MgH_2 + FeTiH/GO (10 h) composite exhibit Avrami exponent values in the range n = 0.7 – 0.9. These moderately low values indicate constrained, diffusion-controlled phase growth with a decreasing nucleation rate [100]. During the second stage of the absorption of the MgH_2 + FeTiH/GO (1 h) and MgH_2 + FeTiH/GO (3 h) samples, even smaller Avrami exponent values are observed ($0.4 < n < 0.6$), reflecting to a slowdown of the reaction relative to the initial stage.

The desorption reactions show similar trends, i.e. for all powders, the first-stage Avrami exponent ranges from $n = 1.0$ to $n = 1.5$ (see Table 2), which is consistent with a constrained, diffusion-driven phase transformation with a decreasing nucleation rate [100]. The second stage proceeds more slowly, with $n \approx 0.4$–0.5, as hydrogen at this point diffuses from deeper within the bulk material.

Phase evolution during dehydrogenation and hydrogenation of the MgH_2 + FeTiH/GO nanopowders is summarized in Fig. 14. Each graph displays the X-ray diffractograms corresponding to the as-milled powder composite, the desorbed state (after a full sorption cycle) and the subsequent absorbed state. At a first glance, the XRD patterns of the

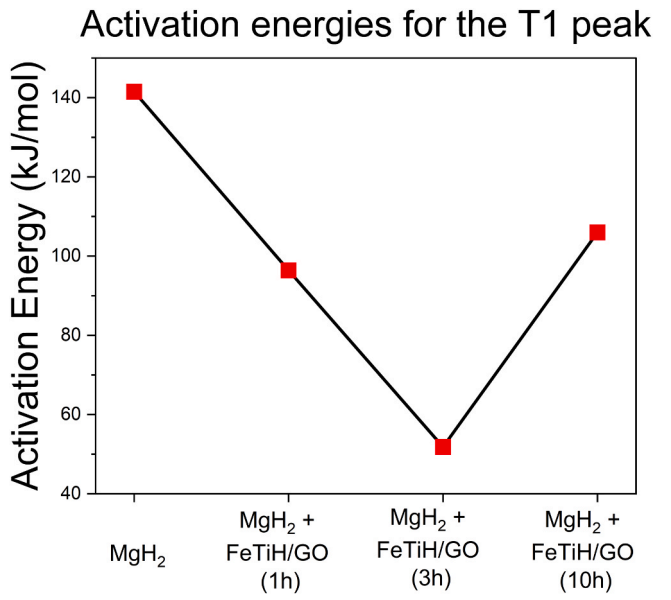

Fig. 11. Activation energies of the MgH_2 (3 h) powder and catalyzed samples.

desorbed states are dominated by the Bragg-peaks of hexagonal Mg, however, minor residual α-MgH_2 peaks are still detectable in this state, indicating that a small fraction of MgH_2 remained unconverted during dehydrogenation. It is important to note that all XRD patterns are presented on a logarithmic scale to emphasize the presence of minor phases. The unchanged intensity of the MgO reflections throughout the hydrogen cycling confirms that no additional oxidation occurred during the PCT measurements. Therefore, the MgO most likely formed during the HEBM process, when fresh internal surfaces were created, and/or during powder containment under protective Ar atmosphere in a glove box, prior to the PCT measurements. This oxide layer plays a significant role only in the case of the MgH_2 + FeTiH/GO (10 h) composite, when an activation cycle is required prior to a reasonable absorption measurement. A notable sharpening of the main Mg phase reflections is observed in the desorbed powders, suggesting the formation of larger nanocrystals during the dehydrogenation process. Upon rehydrogenation, the absorbed powders exhibit the formation of α-MgH_2, while no detectable traces of the high-pressure γ-MgH_2 are observed. CMWP analysis was performed on the X-ray patterns of both the dehydrided and hydrided states, and the resulting microstructural parameters are presented in Fig. 15.

Fig. 15a clearly shows that dehydrogenation after a complete sorption cycle at T = 300 °C does not degrade the nanocrystalline structure of the MgH_2 + FeTiH/GO powder composites, which is critical for their potential practical applications. The main crystalline phase (hexagonal Mg) characterizing this state exhibits a crystallite size ranging from ~35 nm (MgH_2 + FeTiH/GO (10 h)) to ~100 nm (MgH_2 + FeTiH/GO (10 h)). The slight difference in the MgH_2 coherent crystallite size observed in the as-milled powders (see Fig. 8a) is retained throughout the MgH_2 (tetragonal) → Mg (hexagonal) → MgH_2 (tetragonal) → Mg (hexagonal) reaction cycle, resulting in the nucleation of Mg nanocrystals with different size. As confirmed by the XRD patterns (see Fig. 13), these Mg nanocrystals almost fully disappear during the subsequent Mg (hexagonal) → MgH_2 (tetragonal) absorption reaction, while the newly nucleated α-MgH_2 nanocrystals exhibit crystallite size below 40 nm, confirming microstructural stability during hydrogen sorption cycling. Such nanoparticles can contain grain boundaries with a volume fraction of ~10 %, therefore hydrogen diffusion can still be favorable [101]. Specifically, after two complete sorption cycles, the crystallite size of α-MgH_2 in the MgH_2 + FeTiH/GO (1 h) composite is approximately four times larger than in the as-milled state (from $\langle D \rangle_{area} = 8$ nm to $\langle D \rangle_{area} = 35$ nm), whereas the original nanostructure is better

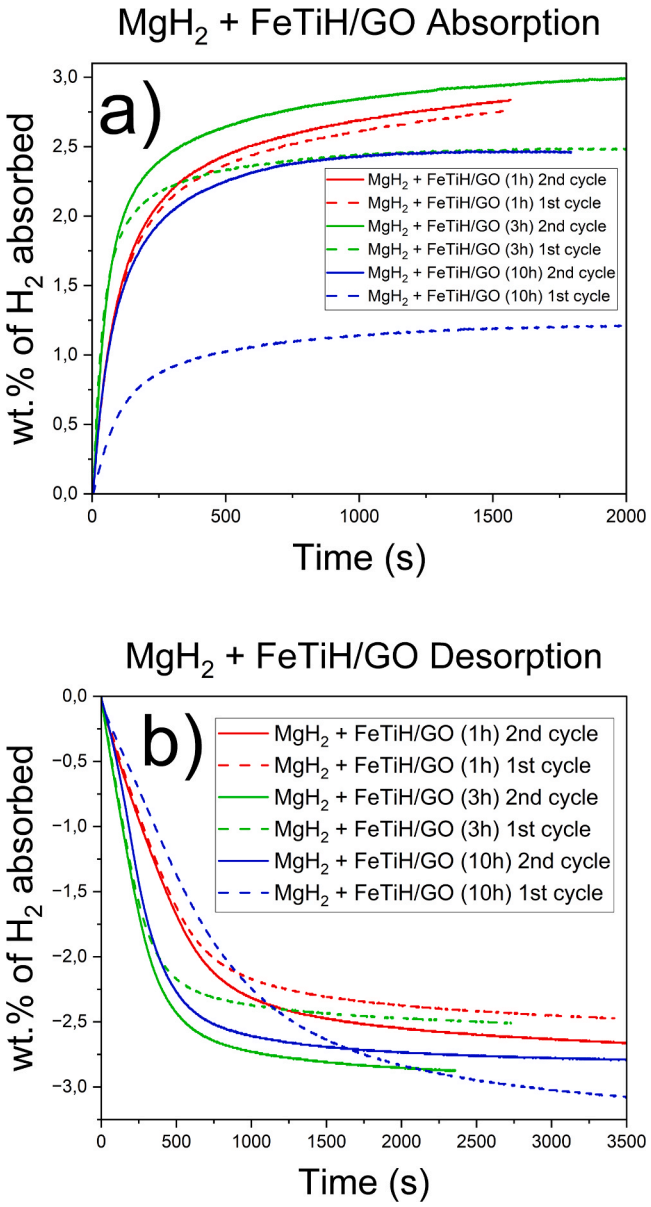

Fig. 12. Hydrogen (a) absorption and (b) desorption curves obtained for the MgH_2 + FeTiH/GO composites.

preserved in the MgH_2 + FeTiH/GO (10 h) sample with only a twofold increase in crystallite size (from $\langle D \rangle_{area} = 5$ nm to $\langle D \rangle_{area} = 12$ nm). Upon dehydrogenation, the dislocation density in hexagonal Mg is an order of magnitude smaller ($\rho \approx 0.3–0.6 \cdot 10^{15}$ m^{-2}) compared to the as-milled powders, but remains relatively high (see Fig. 15b). Subsequent absorption does not significantly alter the value of ρ. The obtained L_C values (30–50 nm) are comparable to the respective $\langle D \rangle_{area}$ values, indicating that, in both the hydrided and dehydrided states, (nearly) every nanocrystal still contains dislocation.

4. Discussion

As demonstrated by the DSC study (see Fig. 9), the addition of FeTiH + GO catalyst to MgH_2 leads to a significant reduction in the T_{onset}, T_1 and T_2 desorption temperatures. In comparison, a GO-free MgH_2 + 40 wt% FeTiH nanocrystalline powder exhibits higher characteristic temperatures [74] than those obtained in this work, highlighting the beneficial effect of GO in enhancing the dehydrogenation performance of MgH_2 + FeTiH/GO composites. These observations are consistent

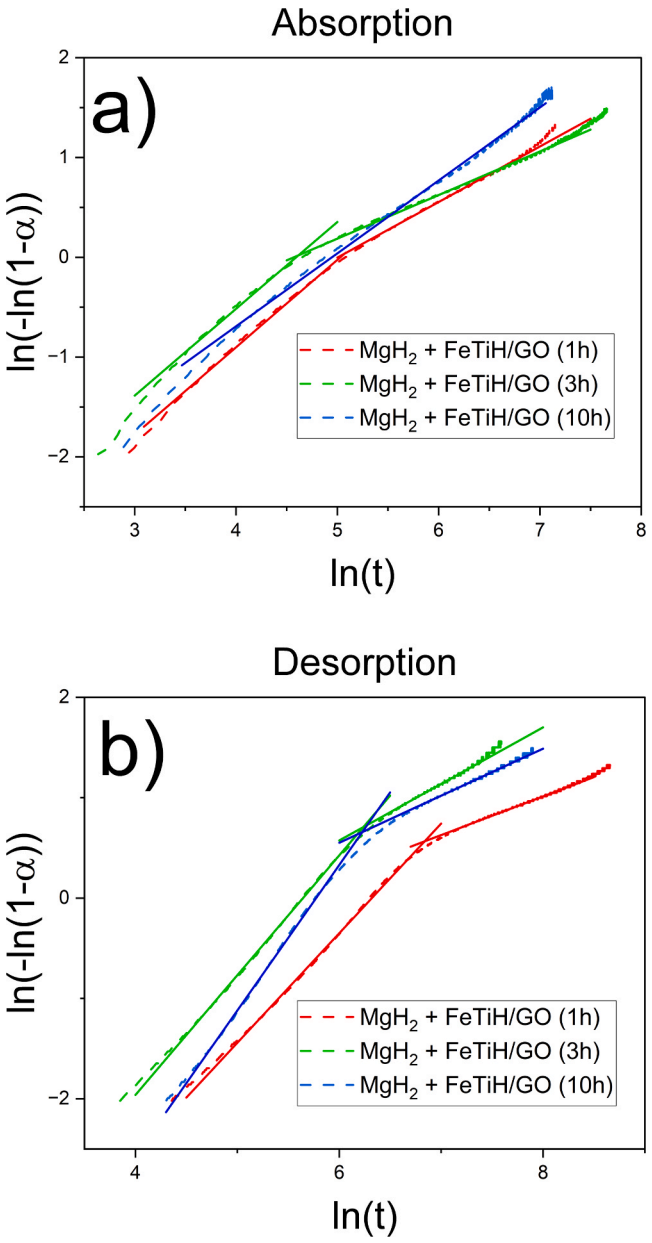

Fig. 13. Double logarithm JMAK plots for (a) absorption and (b) desorption of the MgH_2 + FeTiH/GO powders.

Table 2
Absorption and desorption Avrami-exponents determined from the JMAK analysis of the of MgH_2 + FeTiH/GO composites.

Sample Name	Absorption exponent (n)		Desorption exponent (n)	
MgH_2 + FeTiH/GO (1 h)	0.88	0.56	1.09	0.39
MgH_2 + FeTiH/GO (3 h)	0.87	0.44	1.19	0.56
MgH_2 + FeTiH/GO (10 h)			1.45	0.47
	0.73			

with the work of Mukta et al. as well, who reported that the onset temperature for MgH_2 catalyzed by GO-supported SnO_2 nanoparticles is significantly lower than that of MgH_2 + SnO_2. This behavior was attributed to the catalytic role of GO in destabilizing the Mg-H bond [89]. Furthermore, the distinct T_1 and T_2 peaks observed in the thermogram of the MgH_2 + 40 wt% FeTiH composite [74] become substantially overlapped in the DSC-curve of the MgH_2 + FeTiH/GO (3 h) sample (see Fig. 9) due to peak broadening. The broadening of the first

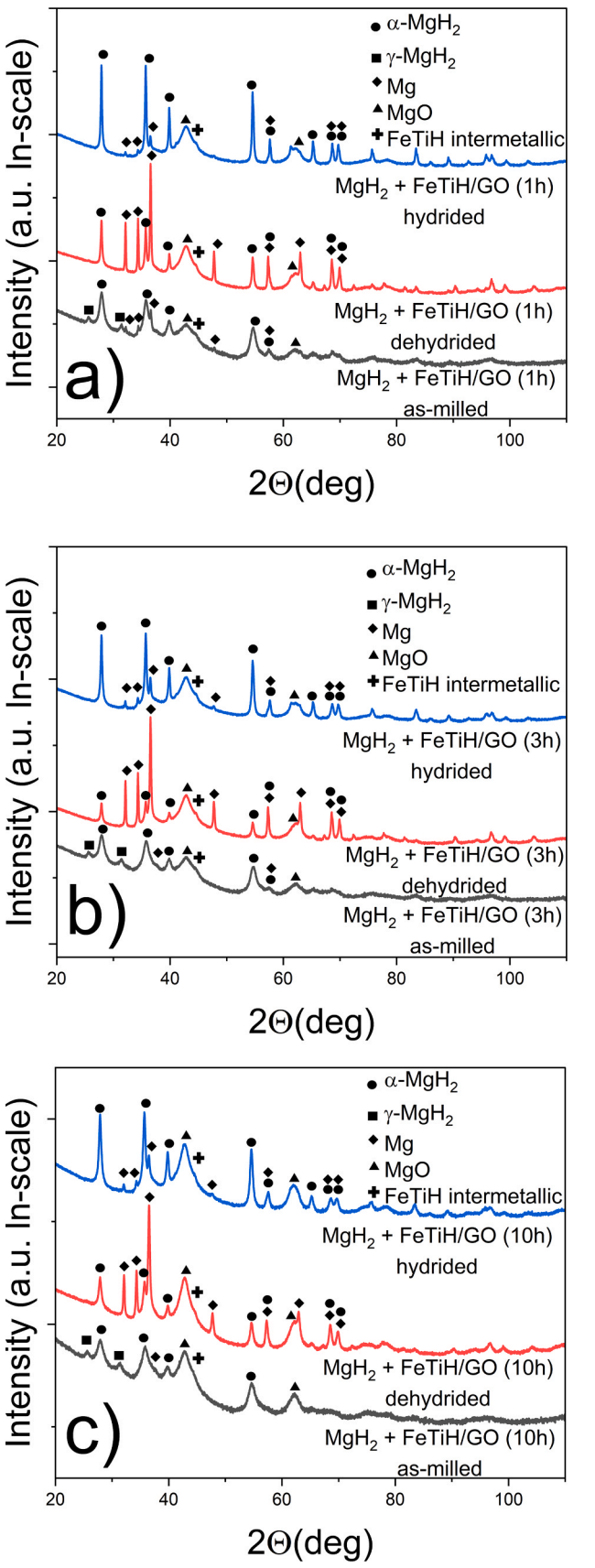

Fig. 14. XRD pattern corresponding to the as-milled, dehydrided and hydrided states of the MgH_2 + FeTiH/GO powders ball-milled for (a) 1 h, (b) 3 h and (c) 10 h.

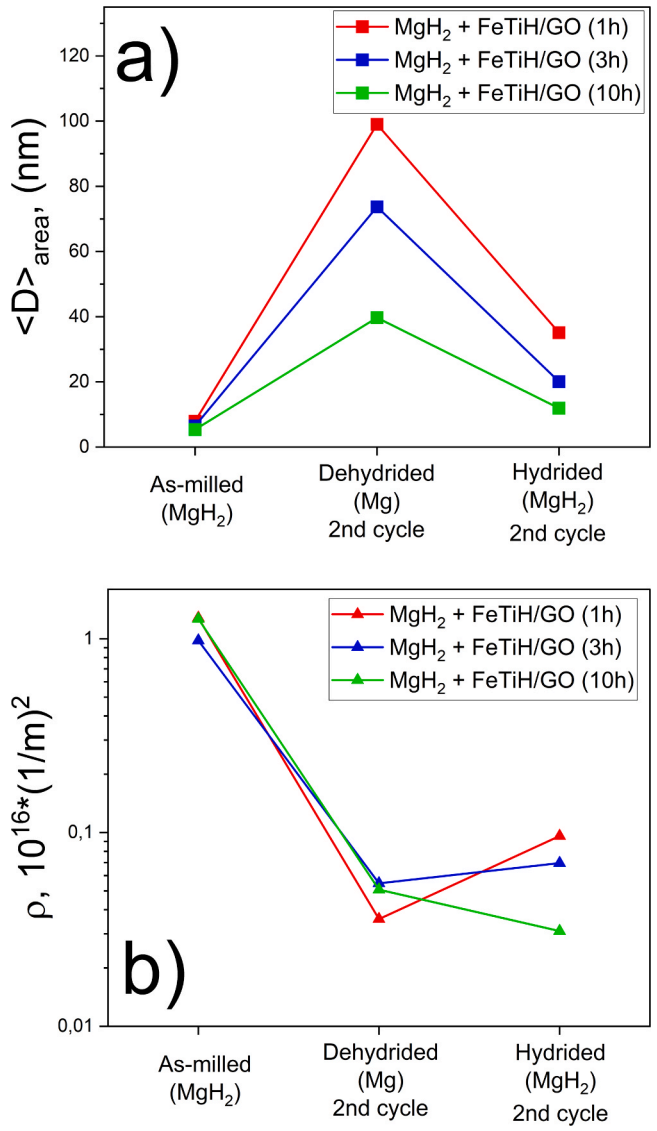

Fig. 15. Structural parameters obtained from the CMPW analysis of the dehydrided and hydrided states of the as-milled MgH_2 and MgH_2 + FeTiH/GO composites. (a) average crystallite.

endothermic reaction, expressed as $\Delta T = T_1 - T_{onset}$ is $\Delta T = 51$ K for MgH_2 + FeTiH/GO (3 h), while it is only $\Delta T = 36$ K for MgH_2 + 40 wt% FeTiH (3 h) [74]. This broadening together with the substantial reduction in T_{onset} confirms the noticeable impact of GO in destabilizing the hydride phase, thereby enhancing the desorption performance of the composite.

Fig. 11 confirmed that the MgH_2 + FeTiH/GO (3 h) sample exhibits the lowest activation energy for the dehydrogenation reaction and. Consistently, PCT measurements demonstrate that this sample kinetically outperforms 1 h and 10 h HEBMed powders, both during hydrogen absorption and desorption (see Fig. 12). These results suggest that there exists an optimal milling time of 3 h, corresponding to a favorable microstructure and morphology of the MgH_2 + FeTiH/GO system. Similar observations have been found for ball-milled nanocrystalline MgH_2 catalyzed by metal-oxide additives [102]. The relatively high FeTiH catalyst content employed in this study may accelerate the hydrogenation and dehydrogenation kinetics at lower temperatures, which is the focus of future research.

The CMWP analysis clearly confirmed that as a result of SPD, the as-milled powders exhibits a fine nanocrystalline structure with extremely high dislocation densities (see Fig. 8a). Hydrogen cycling was found to induce only a moderate increase in the crystallite size of α-MgH_2 – approximately twofold for MgH_2 + FeTiH/GO (10 h), threefold for MgH_2 + FeTiH/GO (3 h), and fourfold for MgH_2 + FeTiH/GO (1 h) – while preserving the nanostructure of the composite powders (see Fig. 15a). Thus, cycling stability of the microstructure of the MgH_2 correlates with the HEBM time, i.e. longer the milling yields a more stable the microstructure. A similar structural stability after several cycles has also been reported for HEBM-processed MgH_2 powder [29]. For each powder composite, the dislocation density decreases by roughly an order of magnitude from 10^{16} m^{-2} to 10^{15} m^{-2} (see Fig. 15b). These observations indicate that the addition of FeTiH/GO catalysts to MgH_2 by ball-milling does not significantly alter the MgH_2 microstructure during phase transformations via subsequent dehydrogenation and hydrogenation. Consequently, the overall hydrogen kinetics performance of the MgH_2 + FeTiH/GO system (see Fig. 12) does not correlate directly with the raw structural parameters obtained from the CMWP analysis, Other morphological features, however, appear to play a significant role in the observed sorption behavior. For example, HRTEM images revealed that FeTi catalyst nanocrystals can be embedded within the MgH_2 matrix in the MgH_2 + FeTiH/GO (3 h) composite powder (see Fig. 4). This morphological feature correlates well with the corresponding EDS spectra (see Fig. 3) and the obtained Mg:Fe-Ti ratio, which is smaller than the nominal value (see Table 1). Consequently, some catalyst particles are partially shielded from the electron beam, consistent with the observed embedded structure. This distinctive morphology likely contributes to the superior kinetic performance of the MgH_2 + FeTiH/GO (3 h) composite.

5. Conclusions

In this work HEBM was applied to synthesize MgH_2 + FeTiH/GO powder composites. The Fe:TiH_2 weight ratio was chosen as 1:1, while the total catalyst content was set as 30 wt%.

TEM study revealed that catalyst nanoparticle is a homogeneous mixture of Fe and Ti and completely wrapped by GO additive. HAADF image of the MgH_2 + FeTiH/GO (3 h) composite demonstrated that FeTi catalyst particles can be embedded inside hydride aggregates, which was further confirmed by EDS analysis, i.e. Mg:FeTi ratio reaches the nominal content of FeTi after 10 h of HEBM.

XRD experiments showed that each composite is dominated by α-MgH_2, however, the high pressure γ-MgH_2 phase is also present. It was obtained from the CMWP X-ray line profile analysis that as-milled powders exhibit a fine nanocrystalline structure ($\langle D \rangle_{area} \sim$ 6–8 nm) an extremely high dislocation density ($\rho \sim 10^{16}$ m^{-2}).

DSC experiments revealed a two-step dehydrogenation process for all powders, corresponding to the H-release of the γ-MgH_2 and α-MgH_2 phases. The addition of FeTiH + GO catalyst to MgH_2 by HEBM leads to a significant reduction in the T_{onset}, T_1 and T_2 desorption temperatures, confirming that GO has a remarkable impact on the destabilization of the hydrides. It was also found that the dehydrogenation activation energy decreased by 65 % for the the MgH_2 + FeTiH/GO (1 h) if compared to pure MgH_2. Isothermal sorption measurements indicated that all powders exhibit good kinetics. Specifically, the initial hydrogen uptake of the MgH_2 + FeTiH/GO (1 h) powder reaches 50 % of the absorbed hydrogen within 100 s. Overall, the fastest absorption and desorption were observed for the MgH_2 + FeTiH/GO (3 h) powder.

The CMWP analysis undoubtedly confirmed that dehydrogenation after a complete sorption cycle does not degrade the nanocrystalline structure of the powder composites, i.e. the crystallite size of α-MgH_2 is only 2–4 times larger than in the as-milled state, coupled with a remarkable high dislocation density ($\rho \sim 10^{15}$ m^{-2}).

CRediT authorship contribution statement

Roman Paramonov: Writing – original draft, Investigation, Formal analysis, Data curation. **Zoltán Novák:** Supervision, Methodology.

János Kele-Jókuthy: Investigation. **Viktória Kovács-Kis:** Investigation, Data curation. **Gábor Ribárik:** Methodology, Formal analysis. **Ádám Révész:** Writing – review & editing, Writing – original draft, Supervision, Methodology, Investigation, Conceptualization. **Tony Spassov:** Supervision, Resources, Investigation, Funding acquisition. **Stanislava Todorova:** Methodology, Investigation. **Zoltán Dankházi:** Visualization, Investigation.

Declaration of Competing Interest

The authors declare that they have no known competing financial interests or personal relationships that could have appeared to influence the work reported in this paper.

Acknowledgement

The authors acknowledge the support of the National Research, Development and Innovation Fund of Hungary under project No. NKFIH-ADVANCED-153100. The electron microscopy facility at the Centre for Energy Research was granted by the European Structural and Investment Funds, grant no. VEKOP-2.3.3–15–2016–0 0 0 02. ZN acknowledges the support of Hungarian Academy of Sciences (Lendület LP2023–12/2023). Research equipment of the project N⁰ BG16RFPR002–1.014–0006 "National Centre of Excellence Mechatronics and Clean Technologies" was used for experimental work financially supported by European Regional Development Fund under "Research Innovation and Digitization for Smart Transformation" program 2021–2027.

Appendix A. Supporting information

Supplementary data associated with this article can be found in the online version at doi:10.1016/j.jallcom.2026.186509.

References

[1] T. Lin, L. Zhang, J. Wan, C.-M. Chen, J. Li, Energy price uncertainty and renewable energy technological innovation: Evidence from listed Chinese firms, Renew. Sustain. Energy Rev. 213 (2025) 115447, https://doi.org/10.1016/j.rser.2025.115447.

[2] H. Ritchie, P. Rosado, M. Roser, Energy Production and Consumption, Our World in Data (2024). ⟨https://ourworldindata.org/energy-production-consumption⟩ (accessed December 30, 2025).

[3] S.G. Nnabuife, A.K. Hamzat, J. Whidborne, B. Kuang, K.W. Jenkins, Integration of renewable energy sources in tandem with electrolysis: A technology review for green hydrogen production, Int. J. Hydrog. Energy 107 (2025) 218–240, https://doi.org/10.1016/j.ijhydene.2024.06.342.

[4] K. Brindhadevi, S.K. Kamarudin, A. Pugazhendhi, Challenges and future directions to improve the hydrogen economy, Renew. Energy 256 (2026) 124560, https://doi.org/10.1016/j.renene.2025.124560.

[5] M. Ning, Y. Yao, Y. Zhan, F. Pan, Y. Fu, D. Chen, M. Zi, M. Shi, Hydrogen Production from Marine Renewable Energy: A Review, Energies 18 (2025) 6490, https://doi.org/10.3390/en18246490.

[6] T.T. Le, P. Sharma, B.J. Bora, V.D. Tran, T.H. Truong, H.C. Le, P.Q.P. Nguyen, Fueling the future: A comprehensive review of hydrogen energy systems and their challenges, Int. J. Hydrog. Energy 54 (2024) 791–816, https://doi.org/10.1016/j.ijhydene.2023.08.044.

[7] L. Zhang, C. Jia, F. Bai, W. Wang, S. An, K. Zhao, Z. Li, J. Li, H. Sun, A comprehensive review of the promising clean energy carrier: Hydrogen production, transportation, storage, and utilization (HPTSU) technologies, Fuel 355 (2024) 129455, https://doi.org/10.1016/j.fuel.2023.129455.

[8] I.M.S. Anekwe, S.I. Mustapha, S.O. Akpasi, E.K. Tetteh, A.S. Joel, Y.M. Isa, The hydrogen challenge: addressing storage, safety, and environmental concerns in hydrogen economy, Int. J. Hydrog. Energy 167 (2025) 150952, https://doi.org/10.1016/j.ijhydene.2025.150952.

[9] T. Zhang, J. Uratani, Y. Huang, L. Xu, S. Griffiths, Y. Ding, Hydrogen liquefaction and storage: Recent progress and perspectives, Renew. Sustain. Energy Rev. 176 (2023) 113204, https://doi.org/10.1016/j.rser.2023.113204.

[10] E. Davies, A. Ehrmann, E. Schwenzfeier-Hellkamp, Safety of Hydrogen Storage Technologies, Processes 12 (2024) 2182, https://doi.org/10.3390/pr12102182.

[11] A.S. Mekonnin, K. Wacławiak, M. Humayun, S. Zhang, H. Ullah, Hydrogen Storage Technology, and Its Challenges: A Review, Catalysts 15 (2025) 260, https://doi.org/10.3390/catal15030260.

[12] L. Schlapbach, A. Züttel, Hydrogen-storage materials for mobile applications, Nature 414 (2001) 353–358, https://doi.org/10.1038/35104634.

[13] N.İ. Beyazit, Comparative Study of Hydrogen Storage and Metal Hydride Systems: Future Energy Storage Solutions, Processes 13 (2025) 1506, https://doi.org/10.3390/pr13051506.

[14] C. Drawer, J. Lange, M. Kaltschmitt, Metal hydrides for hydrogen storage – Identification and evaluation of stationary and transportation applications, J. Energy Storage 77 (2024) 109988, https://doi.org/10.1016/j.est.2023.109988.

[15] G. Scarpati, E. Frasci, G. Di Ilio, E. Jannelli, A comprehensive review on metal hydrides-based hydrogen storage systems for mobile applications, J. Energy Storage 102 (2024) 113934, https://doi.org/10.1016/j.est.2024.113934.

[16] T.H. Le, M.P. Kim, C.H. Park, Q.N. Tran, Recent Developments in Materials for Physical Hydrogen Storage: A Review, Mater 17 (2024) 666, https://doi.org/10.3390/ma17030666.

[17] G. Chen, D. Liang, Z. Kang, J. Fan, S. Fan, X. Zhou, Review of Hydrogen Storage in Solid-State Materials, Energies 18 (2025) 2930, https://doi.org/10.3390/en18112930.

[18] Y. Zhang, W. Bu, Q. Liu, J. Hao, Z. Liu, Z. Hu, X. Liang, Recent advances in nanostructure modification to enhance hydrogen storage performance of magnesium-based alloys, J. Alloy. Compd. 1050 (2026) 185723, https://doi.org/10.1016/j.jallcom.2025.185723.

[19] Z. Li, M. Zhang, H. Xu, Revealing the Roles of Heat Transfer, Thermal Dynamics, and Reaction Kinetics in Hydrogenation/Dehydrogenation Processes for Mg-Based Metal Hydride Hydrogen Storage, Energies 18 (2025) 2924, https://doi.org/10.3390/en18112924.

[20] Á. Révész, M. Gajdics, Improved H-Storage Performance of Novel Mg-Based Nanocomposites Prepared by High-Energy Ball Milling: A Review, Energies 14 (2021) 6400, https://doi.org/10.3390/en14196400.

[21] C. Lang, X. Yao, Enhancing hydrogen storage performance of magnesium-based materials: A review on nanostructuring and catalytic modification, J. Magnes. Alloy. (2025), https://doi.org/10.1016/j.jma.2025.01.015.

[22] C. Zheng, B. Liu, D. Zhou, Z. Hou, D. Zhao, A systematic review on nanostructure engineering of Mg/MgH2 for enhanced hydrogen storage performance, Int. J. Hydrog. Energy 160 (2025) 150629, https://doi.org/10.1016/j.ijhydene.2025.150629.

[23] J. Song, J. She, D. Chen, F. Pan, Latest research advances on magnesium and magnesium alloys worldwide, J. Magnes. Alloy. 8 (2020) 1–41, https://doi.org/10.1016/j.jma.2020.02.003.

[24] K. Edalati, E. Akiba, W.J. Botta, Y. Estrin, R. Floriano, D. Fruchart, T. Grosdidier, Z. Horita, J. Huot, H.W. Li, H.J. Lin, Á. Révész, M.J. Zehetbauer, Impact of severe plastic deformation on kinetics and thermodynamics of hydrogen storage in magnesium and its alloys, J. Mater. Sci. Technol. 146 (2023) 221–239, https://doi.org/10.1016/j.jmst.2022.10.068.

[25] H.J. Lin, Y.S. Lu, L.T. Zhang, H.Z. Liu, K. Edalati, Á. Révész, Recent advances in metastable alloys for hydrogen storage: a review, Rare Met 41 (2022) 1797–1817, https://doi.org/10.1007/s12598-021-01917-8.

[26] C. Liu, Z. Yuan, X. Li, X. Man, T. Zhai, Z. Han, T. Li, Y. Zhang, Hydrogen storage capabilities enhancement of MgH_2 nanocrystals, Int. J. Hydrog. Energy 88 (2024) 515–527, https://doi.org/10.1016/j.ijhydene.2024.09.169.

[27] A. Borchloo, K. Nekouee, A review of enhanced hydrogen storage in MgH_2: the role of high-energy reactive ball milling and catalysis, Synth. Sinter. 5 (2025) 200–230, https://doi.org/10.53063/synsint.2025.53296.

[28] T. Sadhasivam, H.-T. Kim, S. Jung, S.-H. Roh, J.-H. Park, H.-Y. Jung, Dimensional effects of nanostructured Mg/MgH_2 for hydrogen storage applications: A review, Renew. Sustain. Energy Rev. 72 (2017) 523–534, https://doi.org/10.1016/j.rser.2017.01.107.

[29] D. Fátay, T. Spassov, P. Delchev, G. Ribárik, Á. Révész, Microstructural development in nanocrystalline MgH_2 during H-absorption/desorption cycling, Int. J. Hydrog. Energy 32 (2007) 2914–2919, https://doi.org/10.1016/j.ijhydene.2006.12.018.

[30] Y. Chen, S. Wu, X. Cai, L. Zhou, Effects of Ball Milling Time on Microstructure and Hydrogen Storage Properties of Mg-Cu9Al4 Composites, J. Mater. Eng. Perform. 34 (2025) 15169–15178, https://doi.org/10.1007/s11665-024-10132-2.

[31] K. Edalati, A. Bachmaier, V.A. Beloshenko, Y. Beygelzimer, V.D. Blank, W. J. Botta, K. Bryła, J. Čížek, S. Divinski, N.A. Enikeev, Y. Estrin, G. Faraji, R. B. Figueiredo, M. Fuji, T. Furuta, T. Grosdidier, J. Gubicza, A. Hohenwarter, Z. Horita, J. Huot, Y. Ikoma, M. Janeček, M. Kawasaki, P. Král, S. Kuramoto, T. G. Langdon, D.R. Leiva, V.I. Levitas, A. Mazilkin, M. Mito, H. Miyamoto, T. Nishizaki, R. Pippan, V.V. Popov, E.N. Popova, G. Purcek, O. Renk, Á. Révész, X. Sauvage, V. Sklenicka, W. Skrotzki, B.B. Straumal, S. Suwas, L.S. Toth, N. Tsuji, R.Z. Valiev, G. Wilde, M.J. Zehetbauer, X. Zhu, Nanomaterials by severe plastic deformation: review of historical developments and recent advances, Mater. Res. Lett. 10 (2022) 163–256, https://doi.org/10.1080/21663831.2022.2029779.

[32] C. Suryanarayana, Mechanical alloying and milling, Prog. Mater. Sci. 46 (2001) 1–184, https://doi.org/10.1016/S0079-6425(99)00010-9.

[33] K. Edalati, A.Q. Ahmed, S. Akrami, K. Ameyama, V. Aptukov, R.N. Asfandiyarov, M. Ashida, V. Astanin, A. Bachmaier, V. Beloshenko, E.V. Bobruk, K. Bryła, J. M. Cabrera, A.P. Carvalho, N.Q. Chinh, I.C. Choi, R. Chulist, J.M. Cubero-Sesin, G. Davdian, M. Demirtas, S. Divinski, K. Durst, J. Dvorak, P. Edalati, S. Emura, N. A. Enikeev, G. Faraji, R.B. Figueiredo, R. Floriano, M. Fouladvind, D. Fruchart, M. Fuji, H. Fujiwara, M. Gajdics, D. Gheorghe, L. Gondek, J.E. González-Hernández, A. Gornakova, T. Grosdidier, J. Gubicza, D. Gunderov, L. He, O. F. Higuera, S. Hirosawa, A. Hohenwarter, Z. Horita, J. Horky, Y. Huang, J. Huot, Y. Ikoma, T. Ishihara, Y. Ivanisenko, J. il Jang, A.M. Jorge, M. Kawabata-Ota, M. Kawasaki, T. Khelfa, J. Kobayashi, L. Kommel, A. Korneva, P. Kral, N. Kudriashova, S. Kuramoto, T.G. Langdon, D.H. Lee, V.I. Levitas, C. Li, H.W. Li, Y. Li, Z. Li, H.J. Lin, K.D. Liss, Y. Liu, D.M.M. Cardona, K. Matsuda, A. Mazilkin,

Y. Mine, H. Miyamoto, S.C. Moon, T. Müller, J.A. Muñoz, M.Y. Murashkin, M. Naeem, M. Novelli, D. Olasz, R. Pippan, V.V. Popov, E.N. Popova, G. Purcek, P. de Rango, O. Renk, D. Retraint, Á. Révész, V. Roche, P. Rodriguez-Calvillo, L. Romero-Resendiz, X. Sauvage, T. Sawaguchi, H. Sena, H. Shahmir, X. Shi, V. Sklenicka, W. Skrotzki, N. Skryabina, F. Staab, B. Straumal, Z. Sun, M. Szczerba, Y. Takizawa, Y. Tang, R.Z. Valiev, A. Vozniak, A. Voznyak, B. Wang, J.T. Wang, G. Wilde, F. Zhang, M. Zhang, P. Zhang, J. Zhou, X. Zhu, Y.T. Zhu, Severe plastic deformation for producing superfunctional ultrafine-grained and heterostructured materials: An interdisciplinary review, J. Alloy. Compd. 1002 (2024), https://doi.org/10.1016/j.jallcom.2024.174667.

[34] A. Bnihoum, M. EL Kassaoui, A. Razouk, H. Ez-zahraouy, O. Mounkachi, Strain engineering of substitutionally doped MgH_2 as a hydrogen storage medium: Thermodynamic and diffusion kinetics investigation, Int. J. Hydrog. Energy 146 (2025) 149974, https://doi.org/10.1016/j.ijhydene.2025.06.164.

[35] N. Skryabina, V. Aptukov, D. Fruchart, Role of induced elastic deformations at the Mg/MgH2 transformation, J. Alloy. Metall. Syst. 5 (2024) 100064, https://doi.org/10.1016/j.jalmes.2024.100064.

[36] Á. Révész, D. Fátay, Microstructural evolution of ball-milled MgH_2 during a complete dehydrogenation–hydrogenation cycle, J. Power Sources 195 (2010) 6997–7002, https://doi.org/10.1016/j.jpowsour.2010.04.085.

[37] J. Grbović Novaković, N. Novaković, S. Kurko, S. Milošević Govedarović, T. Pantić, B. Paskaš Mamula, K. Batalović, J. Radaković, J. Rmuš, M. Shelyapina, N. Skryabina, P. deRango, D. Fruchart, Influence of Defects on the Stability and Hydrogen-Sorption Behavior of Mg-Based Hydrides, ChemPhysChem 20 (2019) 1216–1247, https://doi.org/10.1002/cphc.201801125.

[38] Á. Révész, M. Gajdics, The Effect of Severe Plastic Deformation on the Hydrogen Storage Properties of Metal Hydrides, Mater. Trans. 64 (2023) 1387–1400, https://doi.org/10.2320/matertrans.MT-MF2022019.

[39] M. EL Hayany, M. EL Kassaoui, A. Benyoussef, J.-M. Nunzi, O. Mounkachi, Theoretical approach to study hydrogen storage properties of MgH_2 nanoclusters: Crucial role of hydrogen kinetics, Int. J. Hydrog. Energy 201 (2026) 152960, https://doi.org/10.1016/j.ijhydene.2025.152960.

[40] A. Li, Q. Fang, W. Sun, Z. Yuan, Y. Han, Catalytic mechanism of hydrogen absorption and desorption reactions in Mg-based hydrogen storage materials, J. Alloy. Compd. 1038 (2025) 182814, https://doi.org/10.1016/j.jallcom.2025.182814.

[41] L. Dan, H. Wang, X. Yang, J. Liu, L. Ouyang, M. Zhu, Low-temperature solid-state hydrogen storage via efficiently catalyzed MgH_2, Renew. Energy 231 (2024) 121009, https://doi.org/10.1016/j.renene.2024.121009.

[42] H. Chu, H. Li, S. Qiu, Y.S. Chua, C. Yin, H. Huang, Y. Li, Y. Zou, F. Xu, L. Sun, High-efficiency hydrogen storage of magnesium hydride achieved by catalytic doping with zirconium titanate, J. Energy Storage 114 (2025) 115907, https://doi.org/10.1016/j.est.2025.115907.

[43] W. Luo, C. Xu, K. Wang, Y. Ma, Z. Wu, C. Zhao, Y. He, S. Sun, H. Leng, C. Sun, Q. Li, C. Wu, Multivalent Ti/Nb catalysts with oxygen vacancies: Bridging electron transfer pathways to enhance MgH_2 hydrogen desorption property, J. Alloy. Compd. 1031 (2025) 181070, https://doi.org/10.1016/j.jallcom.2025.181070.

[44] R. Shahi, A. Tiwari, M. Shaz, O.N. Srivastava, Studies on de/rehydrogenation characteristics of nanocrystalline MgH2 co-catalyzed with Ti, Fe and Ni, Int. J. Hydrog. Energy 38 (2013) 2778–2784, https://doi.org/10.1016/j.ijhydene.2012.11.073.

[45] M.F. Saeid, B.A. Abdulkadir, M. Ismail, H.D. Setiabudi, Enhanced hydrogen storage properties of MgH_2 through doping with titanium-based catalyst materials: A review and bibliometric analysis, Mater. Sci. Semicond. Process 200 (2025) 109931, https://doi.org/10.1016/j.mssp.2025.109931.

[46] H. Guan, J. Liu, X. Sun, Y. Lu, H. Wang, Q. Luo, Q. Li, F. Pan, Titanium-Nickel Dual Active Sites Enabled Reversible Hydrogen Storage of Magnesium at 180 °C with Exceptional Cycle Stability, Adv. Mater. 37 (2025) e2500178, https://doi.org/10.1002/adma.202500178.

[47] S. Li, L. Zhang, F. Wu, Y. Jiang, X. Yu, Efficient catalysis of FeNiCu-based multi-site alloys on magnesium-hydride for solid-state hydrogen storage, Chin. Chem. Lett. 36 (2025) 109566, https://doi.org/10.1016/j.cclet.2024.109566.

[48] Q. Hou, Q. Wang, X. Du, Z. Xu, X. Xu, Y. Zhou, Z. Ding, Fe-Based Catalysts in MgH_2 Hydrogen Storage: Mechanistic Insights, Stability Challenges, and a Roadmap for Scalable Design, Coatings 16 (2026) 92, https://doi.org/10.3390/coatings16010092.

[49] Á. Révész, M. Gajdics, T. Spassov, Microstructural evolution of ball-milled Mg–Ni powder during hydrogen sorption, Int. J. Hydrog. Energy 38 (2013) 8342–8349, https://doi.org/10.1016/j.ijhydene.2013.04.128.

[50] X. Zhang, S. Ju, C. Li, J. Hao, Y. Sun, X. Hu, W. Chen, J. Chen, L. He, G. Xia, F. Fang, D. Sun, X. Yu, Atomic reconstruction for realizing stable solar-driven reversible hydrogen storage of magnesium hydride, Nat. Commun. 15 (2024) 2815, https://doi.org/10.1038/s41467-024-47077-y.

[51] T. Zhong, T. Xu, L. Zhang, F. Wu, Y. Jiang, X. Yu, Designing multivalent NiMn-based layered nanosheets with high specific surface area and abundant active sites for solid-state hydrogen storage in magnesium hydride, J. Magnes. Alloy. 13 (2025) 148–160, https://doi.org/10.1016/j.jma.2024.04.027.

[52] V.N. Kudiiarov, A. Kenzhiyev, N. Kurdyumov, R.R. Elman, L.A. Svyatkin, D. V. Terenteva, Superior catalytic activity of nano sized Ni produced by electrical explosion of wires towards the hydrogen storage of magnesium hydride, Int. J. Hydrog. Energy 109 (2025) 436–452, https://doi.org/10.1016/j.ijhydene.2025.01.495.

[53] X. Liu, X. Meng, T. Zhong, Y. Wang, F. Wu, H. Liu, H. Li, L. Zhang, Polymeric carbon nitride supported single-phase Ni with exceptional catalytic effect on MgH2 for hydrogen storage, J. Alloy. Compd. 1032 (2025) 181259, https://doi.org/10.1016/j.jallcom.2025.181259.

[54] M. Gajdics, T. Spassov, V.K. Kis, E. Schafler, Á. Révész, Microstructural and morphological investigations on Mg-Nb_2O_5-CNT nanocomposites processed by high-pressure torsion for hydrogen storage applications, Int. J. Hydrog. Energy 45 (2020) 7917–7928, https://doi.org/10.1016/j.ijhydene.2019.06.165.

[55] G. Barkhordarian, T. Klassen, R. Bormann, Fast hydrogen sorption kinetics of nanocrystalline Mg using Nb_2O_5 as catalyst, Scr. Mater. 49 (2003) 213–217, https://doi.org/10.1016/S1359-6462(03)00259-8.

[56] Y. Qin, J. Hu, Z. Yang, C. Han, S. Long, D. Zhang, Y. Chen, F. Pan, Constructing VO/V_2O_3 interface to enhance hydrogen storage performance of MgH_2, J. Magnes. Alloy. 12 (2024) 4877–4886, https://doi.org/10.1016/j.jma.2024.02.012.

[57] L. Wang, L. Zhang, F. Wu, Y. Jiang, Z. Yao, L. Chen, Promoting catalysis in magnesium hydride for solid-state hydrogen storage through manipulating the elements of high entropy oxides, J. Magnes. Alloy. 12 (2024) 5038–5050, https://doi.org/10.1016/j.jma.2024.01.030.

[58] M. Yang, R. Zhou, Y. Wang, F. Wu, H. Liu, H. Li, L. Zhang, Incorporating in-situ formed Ti^{3+} and oxygen vacancies to TiO_2 via Ni loading for superior hydrogen storage in magnesium hydride, Int. J. Hydrog. Energy 169 (2025) 151158, https://doi.org/10.1016/j.ijhydene.2025.151158.

[59] Y. Chu, F. Cheng, Y. Zheng, L. Jiang, G. Gao, C. Lv, C. Li, G. Wu, M. Fan, Z. Yao, Effect of porous nanosheet NiO on hydrogen storage performance of MgH_2, J. Alloy. Compd. 1050 (2026) 185544, https://doi.org/10.1016/j.jallcom.2025.185544.

[60] T. Tian, F. Liu, X. Zhang, J. Wang, S. Li, W. Chen, Y. Song, J. Li, G. Liu, Effect of porous nanosheet NiO on hydrogen storage performance of MgH_2, Int. J. Hydrog. Energy 135 (2025) 2–9, https://doi.org/10.1016/j.ijhydene.2025.05.017.

[61] Y.K. Yadav, M.A. Shaz, T.P. Yadav, Notable catalytic activity of Al–Cu–Fe–Ni–Cr high entropy alloy nanoparticles for hydrogen sorption in MgH_2, Int. J. Hydrog. Energy 141 (2025) 935–945, https://doi.org/10.1016/j.ijhydene.2025.02.361.

[62] S. Yan, L. Wei, Y. Gong, K. Yang, Enhanced hydrogen storage properties of magnesium hydride by multifunctional carbon-based materials: A review, Int. J. Hydrog. Energy 55 (2024) 521–541, https://doi.org/10.1016/j.ijhydene.2023.11.219.

[63] J. Wu, Z. Liu, H. Zhang, Y. Zou, B. Li, C. Xiang, L. Sun, F. Xu, T. Yu, Hydrogen storage performance of MgH2 under catalysis by highly dispersed nickel-nanoparticle–doped hollow spherical vanadium nitride, J. Magnes. Alloy. 12 (2024) 5132–5143, https://doi.org/10.1016/j.jma.2023.11.010.

[64] X. Zhang, Y. Liu, Z. Ren, X. Zhang, J. Hu, Z. Huang, Y. Lu, M. Gao, H. Pan, Realizing 6.7 wt% reversible storage of hydrogen at ambient temperature with non-confined ultrafine magnesium hydrides, Energy Environ. Sci. 14 (2021) 2302–2313, https://doi.org/10.1039/D0EE03160G.

[65] Y. Chen, X. Li, B. Sun, G. Zhang, S. Ni, C. Li, Effect of NiFe-LDH/FeO(OH) derivatives on the hydrogen storage properties of MgH_2, Int. J. Hydrog. Energy 121 (2025) 326–336, https://doi.org/10.1016/j.ijhydene.2025.03.367.

[66] F. Liu, J. Wang, W. Chen, X. Zhang, S. Li, J. Li, Y.-F. Song, J. Chu, G. Liu, In-situ formed Ti/TiH_2 from exfoliated few-layered Ti3C2Tx as hydrogen pump enhances the hydrogen storage properties of MgH_2, J. Colloid Interface Sci. 700 (2025) 138335, https://doi.org/10.1016/j.jcis.2025.138335.

[67] Z. Deng, R. Zhou, D. Chen, F. Wu, H. Li, L. Zhang, Carbon-doped TiO_2 supported with NiCr particles: a significant boost to MgH_2 for hydrogen storage, J. Energy Storage 136 (2025) 118530, https://doi.org/10.1016/j.est.2025.118530.

[68] H. Emami, K. Edalati, J. Matsuda, E. Akiba, Z. Horita, Hydrogen storage performance of TiFe after processing by ball milling, Acta Mater. 88 (2015) 190–195, https://doi.org/10.1016/j.actamat.2014.12.052.

[69] H. Leng, Z. Yu, J. Yin, Q. Li, Z. Wu, K.-C. Chou, Effects of Ce on the hydrogen storage properties of TiFe0.9Mn0.1 alloy, Int. J. Hydrog. Energy 42 (2017) 23731–23736, https://doi.org/10.1016/j.ijhydene.2017.01.194.

[70] H. Shang, P. Sheng, J. Li, W. Zhang, X. Zhang, S. Guo, Y. Li, Y. Zhang, Characteristics of hydrogen storage of as-milled TiFe-based alloys, Int. J. Hydrog. Energy (2023) 190–200, https://doi.org/10.1016/j.ijhydene.2023.06.325.

[71] V.Yu Zadorozhnyy, S.N. Klyamkin, S.D. Kaloshkin, M.Yu Zadorozhnyy, O. V. Bermesheva, Mechanochemical synthesis and hydrogen sorption properties of nanocrystalline TiFe, Inorg. Mater. 47 (2011) 1081–1086, https://doi.org/10.1134/S0020168511100232.

[72] H. Liu, J. Zhang, P. Sun, C. Zhou, Y. Liu, Z.Z. Fang, An overview of TiFe alloys for hydrogen storage: Structure, processes, properties, and applications, J. Energy Storage 68 (2023) 107772, https://doi.org/10.1016/j.est.2023.107772.

[73] P. Modi, K.-F. Aguey-Zinsou, Room Temperature Metal Hydrides for Stationary and Heat Storage Applications: A Review, Front. Energy Res. 9 (2021) 616115, https://doi.org/10.3389/fenrg.2021.616115.

[74] R. Paramonov, T. Spassov, P. Nagy, Á. Révész, Synergetic Effect of FeTi in Enhancing the Hydrogen-Storage Kinetics of Nanocrystalline MgH_2, Energies 17 (2024) 794, https://doi.org/10.3390/en17040794.

[75] Á. Révész, R. Paramonov, T. Spassov, M. Gajdics, Microstructure and Hydrogen Storage Performance of Ball-Milled MgH_2 Catalyzed by FeTi, Energies 16 (2023) 1061, https://doi.org/10.3390/en16031061.

[76] R. Varin, Z. Zaranski, T. Czujko, M. Polanski, Z. Wronski, The composites of magnesium hydride and iron-titanium intermetallic, Int. J. Hydrog. Energy 36 (2011) 1177, https://doi.org/10.1016/j.ijhydene.2010.06.092.

[77] X. Lu, L. Zhang, H. Yu, Z. Lu, J. He, J. Zheng, F. Wu, L. Chen, Achieving superior hydrogen storage properties of MgH_2 by the effect of TiFe and carbon nanotubes, Chem. Eng. J. 422 (2021) 130101, https://doi.org/10.1016/j.cej.2021.130101.

[78] Z. Zaranski, T. Czujko, The influence of ball milling process on hydrogenation properties of MgH_2–$FeTiH_x$ composites, J. Alloy. Compd. 509 (2011) S608–S611, https://doi.org/10.1016/j.jallcom.2010.10.063.
[79] F.J. Antiqueira, D.R. Leiva, G. Zepon, W.J. Botta, Room temperature conversion of Mg to MgH2 assisted by low fractions of additives, Int. J. Hydrog. Energy 47 (2022) 470–489, https://doi.org/10.1016/j.ijhydene.2021.10.047.
[80] T. Kondo, K. Shindo, Y. Sakurai, Dependence of hydrogen storage characteristics of Mg–TiFe 0.92Mn 0.08 composite on amount of TiFe 0.92Mn 0.08, J. Alloy. Compd. 404 (2005) 511–514, https://doi.org/10.1016/j.jallcom.2004.10.090.
[81] K. Iyakutti, R.P. Reji, K. Ajaijawahar, A. Karthigeyan, Y. Kawazoe, Exploring hydrogen storage properties of Graphene-MgH_2 systems: A combined computational and experimental study, Int. J. Hydrog. Energy 139 (2025) 740–752, https://doi.org/10.1016/j.ijhydene.2025.05.215.
[82] P.K. Soni, A. Bhatnagar, V. Shukla, M.A. Shaz, Improved de/re-hydrogenation properties of MgH_2 catalyzed by graphene templated Ti–Ni–Fe nanoparticles, Int. J. Hydrog. Energy 47 (2022) 21391–21402, https://doi.org/10.1016/j.ijhydene.2022.04.264.
[83] L. Ji, L. Zhang, X. Yang, X. Zhu, L. Chen, The remarkably improved hydrogen storage performance of MgH2 by the synergetic effect of an FeNi/rGO nanocomposite, Dalton Trans. 49 (2020) 4146–4154, https://doi.org/10.1039/D0DT00230E.
[84] S.K. Verma, M.A. Shaz, T.P. Yadav, Enhanced hydrogen absorption and desorption properties of MgH_2 with graphene and vanadium disulfide, Int. J. Hydrog. Energy 48 (2023) 21383–21394, https://doi.org/10.1016/j.ijhydene.2021.12.269.
[85] H. Yu, Z. Yuan, Q. Han, J. Li, T. Li, Effect of high-activity Co/CeO2@C on hydrogen storage kinetics of MgH_2, J. Alloy. Compd. 1053 (2026) 186245, https://doi.org/10.1016/j.jallcom.2026.186245.
[86] H. Wang, J. Sun, H. Shang, Breaking kinetic and thermodynamic barriers: CeO_2-Ni-rGO synergistic catalysis for comprehensively enhanced hydrogen storage performance of MgH_2, J. Alloy. Compd. 1052 (2026) 186167, https://doi.org/10.1016/j.jallcom.2026.186167.
[87] A. Kadri, Y. Jia, Z. Chen, X. Yao, Catalytically Enhanced Hydrogen Sorption in Mg-MgH_2 by Coupling Vanadium-Based Catalyst and Carbon Nanotubes, Mater 8 (2015) 3491–3507, https://doi.org/10.3390/ma8063491.
[88] P. Yao, Y. Jiang, Y. Liu, C. Wu, K.-C. Chou, T. Lyu, Q. Li, Catalytic effect of Ni@rGO on the hydrogen storage properties of MgH2, J. Magnes. Alloy. 8 (2020) 461–471, https://doi.org/10.1016/j.jma.2019.06.006.
[89] D.R. Mukta, Md.M. Hasan, Md.Y. Ali, K.M.A.U. Haque, MostA. Khatun, M. J. Uddin, S. Enzo, Md.W. Rahman, Improved in hydrogen storage properties of MgH_2 catalyzed by as-prepared Graphene oxide-supported SnO_2 nanoparticles, Res. Chem. Inter. 50 (2024) 2859–2872, https://doi.org/10.1007/s11164-024-05294-6.
[90] M. Gajdics, T. Spassov, V. Kovács Kis, F. Béke, Z. Novák, E. Schafler, Á. Révész, Microstructural Investigation of Nanocrystalline Hydrogen-Storing Mg-Titanate Nanotube Composites Processed by High-Pressure Torsion, Energies 13 (2020) 563, https://doi.org/10.3390/en13030563.
[91] H.E. Kissinger, Reaction Kinetics in Differential Thermal Analysis, Anal. Chem. 29 (1957) 1702–1706, https://doi.org/10.1021/ac60131a045.
[92] Á. Révész, Á. Pintér, Time-Dependent Multi-Particle Model Describing the Hydrogen Absorption of Nanocrystalline Magnesium Powders: A Case Study, Energies 17 (2024) 2322, https://doi.org/10.3390/en17102322.
[93] P. Wang, A.M. Wang, B.Z. Ding, Z.Q. Hu, Mg–FeTi1.2 (amorphous) composite for hydrogen storage, J. Alloy. Compd. 334 (2002) 243–248, https://doi.org/10.1016/S0925-8388(01)01771-6.
[94] H.Y. Sohn, S. Emami, Kinetics of dehydrogenation of the Mg–Ti–H hydrogen storage system, Int. J. Hydrog. Energy 36 (2011) 8344–8350, https://doi.org/10.1016/j.ijhydene.2011.03.167.
[95] Á. Révész, Zs Kánya, T. Verebélyi, P.J. Szabó, A.P. Zhilyaev, T. Spassov, The effect of high-pressure torsion on the microstructure and hydrogen absorption kinetics of ball-milled $Mg_{70}Ni_{30}$, J. Alloy. Compd. 504 (2010) 83–88, https://doi.org/10.1016/j.jallcom.2010.05.058.
[96] T. Ungár, G. Tichy, J. Gubicza, R.J. Hellmig, Correlation between subgrains and coherently scattering domains, Powder Diffr. 20 (2005) 366–375, https://doi.org/10.1154/1.2135313.
[97] H. Wan, D. Fang, S. Zhou, X. Yang, Y. Dai, L. Ran, Y. Chen, F. Pan, Enhanced dehydrogenation properties and mechanism analysis of MgH_2 solid solution containing Fe nano-catalyst, Int. J. Hydrog. Energy 48 (2023) 34180–34191, https://doi.org/10.1016/j.ijhydene.2023.05.201.
[98] M. Jiang, C. Ge, P. Wu, C. Ni, C. Hou, H. Kimura, W. Du, X. Xie, AlV_3 catalyzed MgH_2 with high hydrogen storage cycle stability, J. Alloy. Compd. 1040 (2025) 183585, https://doi.org/10.1016/j.jallcom.2025.183585.
[99] J. Christian, The Theory of Transformations in Metals and Alloys, Pergamon: Oxford, UK, 1975.
[100] I. Matsumoto, K. Asano, K. Sakaki, Y. Nakamura, Hydrogen absorption kinetics of magnesium fiber prepared by vapor deposition, Int. J. Hydrog. Energy 36 (2011) 14488–14495, https://doi.org/10.1016/j.ijhydene.2011.08.029.
[101] Y. Pang, Y. Liu, M. Gao, L. Ouyang, J. Liu, H. Wang, M. Zhu, H. Pan, A mechanical-force-driven physical vapour deposition approach to fabricating complex hydride nanostructures, Nat. Commun. 5 (2014) 3519, https://doi.org/10.1038/ncomms4519.
[102] D. Fátay, Á. Révész, T. Spassov, Particle size and catalytic effect on the dehydriding of MgH_2, J. Alloy. Compd. 399 (2005) 237–241, https://doi.org/10.1016/j.jallcom.2005.02.043.